REAL-TIME DUAL ENERGY MARKERLESS MONITORING OF LUNG TUMORS USING A CLINICAL ROOM-MOUNTED STEREOSCOPIC AND MONOSCOPIC X-RAY IMAGING SYSTEM

by

Zakary McLure

Submitted in partial fulfilment of the requirements
for the degree of Master of Science

at

Dalhousie University
Halifax, Nova Scotia
August 2024

Dalhousie University is located in Mi'kma'ki, the ancestral and unceded territory of the Mi'kmaq. We are all Treaty people.

DEDICATION

I would like to dedicate this work to my family and close friends, the people who enabled me to persevere through this challenging yet fulfilling endeavour. Your encouragement and belief in me mean the world. Thank you especially to my parents, Cindy and Neil, my brothers, Jayk and Damien, and finally, to Skye. I love you all very much.

TABLE OF CONTENTS

LIST OF TABLES

LIST OF FIGURES

ABSTRACT

This thesis develops real-time dual-energy markerless imaging technology to monitor lung tumor motion using a clinical room-mounted x-ray imaging system to enhance radiotherapy precision. The first chapter introduces the fundamentals of x-ray production, interactions, and imaging system, providing a comprehensive review of x-ray tubes, detectors, and the imaging process.

The second chapter presents a detailed research manuscript focusing on the development of a novel dual-energy tumor localization technique for real-time applications. This work addresses the critical challenge of x-ray beam obstruction by rotating gantries in room-mounted stereoscopic imaging systems. It employs a Gaussian probability density function approach to estimate the 3D position of lung tumors using limited 2D information from single x-ray views, enhancing localization accuracy. The chapter thoroughly discusses the methodologies, experimental findings, and clinical implications, demonstrating that dual-energy imaging improves tumor monitoring success rates, particularly for smaller tumors and in situations where bone obstructions are present. It also explores the integration of other motion prediction algorithms such as the Kalman filter and the application of epipolar constraints to improve 3D localization accuracy.

The final chapter summarizes the key results of the research, re-emphasizing the potential clinical benefits of the developing technique in reducing planning margins and minimizing the treatment of healthy tissues. It also outlines suggested avenues for future research, including immediate next steps based on the findings of the manuscript. Future work involves considering the clinical implementation of the techniques developed in this thesis. This thesis aims to contribute to the advancement of precision radiotherapy by providing a robust technique for real-time, markerless lung tumor monitoring.

LIST OF ABBREVIATIONS USED

4DCT	Four-Dimensional Computed Tomography
A-PDF	Arbitrary-shape PDF
ACNR	Anti-Correlated Noise Reduction
CBCT	Cone-Beam CT
CNR	Contrast-to-Noise Ratio
CR	Computed Radiography
CT	Computed Tomography
CTV	Clinical Target Volume
DE	Dual-Energy
DE-CBCT	Dual-Energy Cone Beam CT
DECT	Dual-Energy CT
DRR	Digitally Reconstructed Radiograph
EM	Electromagnetic
FPD	Flat Panel Detector
G-PDF	Gaussian PDF
GTV	Gross Tumor Volume
HE	High Energy
HPF	High-Pass Filter
HU	Hounsfield Unit
IDC	Interdimensional Correlation
IGRT	Image-Guided Radiation Therapy
II	Image Intensifier
ITV	Internal Target Volume
kV	Kilovoltage
LE	Low Energy
LINAC	Linear Accelerator
MLC	Multileaf Collimator
MV	Megavoltage
NCC	Normalized Cross Correlation
OAR	Organ At Risk
PDF	Probability Density Function
PTV	Planning Target Volume
ROI	Region of Interest

RTTT	Real-Time Tumor Tracking
SAD	Source-Axis Distance
SBRT	Stereotactic Body Radiation Therapy
SDD	Source-Detector Distance
SE	Single-Energy
SNR	Signal-to-Noise Ratio
SRS	Stereotactic Radiosurgery
TFT	Thin-Film Transistor
VMAT	Volumetric Arc Therapy
Z	Atomic Number

ACKNOWLEDGEMENTS

I would like to start by sincerely thanking my committee members, Dr. Chris Thomas and Dr. Alasdair Syme. Their insightful feedback and challenging questions during our meetings have been greatly helpful and appreciated, always keeping me on my toes and encouraging me to think creatively and critically outside the box.

I would also like to offer a special thanks to Chris Peacock, who laid the foundations of this project through his innovative design of the initial experiment. I can truly say that his contributions were essential to the success of this project.

To my fellow classmates Dan, Shahin, Ahmed, and Natali: we made a remarkable team as we progressed through the challenging coursework, providing mutual support and learning a great deal from each other. Your camaraderie and collaboration have been invaluable. Additionally, I extend my thanks to Nick Lynch, whose mentorship allowed my transition into graduate school to be a positive and enriching experience. I wish you all the best in your future endeavours and look forward to seeing all that you will achieve.

Finally, I would like to express my deepest gratitude to my supervisor, Dr. Mike Sattarivand, for the wisdom, guidance, and unwavering support he has provided throughout the past couple of years. His commitment to the success of his students is truly inspiring, and I've been very fortunate to have had the honor of being his student.

.

Chapter 1: Introduction

Imaging for radiotherapy is integral to the precise delivery of radiation to cancerous tumors, optimizing effectiveness while minimizing exposure to healthy tissues during treatment. This specialized discipline harnesses electromagnetic (EM) radiation to produce detailed images essential for guiding therapeutic procedures with precision and efficiency. EM radiation ranges from harmless radio waves to high energy small wavelength x-rays and gamma rays. Imaging makes use of photons in the diagnostic energy range from 20 keV to 150 keV (i.e., x-rays). X-rays are classified as ionizing radiation, meaning that the photon's energy may be sufficient to remove electrons from an atom. Most x-rays are produced when an electron with high kinetic energy interacts with a material and transfers its energy into the form of EM radiation.

Radiotherapy relies on x-rays to penetrate tissues and generate images that help identify the location, dimensions, and morphology of tumors. These images are essential for treatment planning, enabling clinicians to tailor radiation doses to target tumors effectively while minimizing collateral damage to adjacent organs.

The discovery of x-rays by Wilhelm Roentgen in 1895 marked a significant moment in the history of medical science, revolutionizing diagnostic capabilities by enabling non-invasive visualization of internal structures. This breakthrough laid the groundwork for subsequent advancements in medical imaging throughout the decades, including applications in therapeutic contexts such as radiotherapy.

Throughout subsequent decades, x-ray imaging has evolved from rudimentary techniques to sophisticated systems tailored specifically to radiotherapy. Modern x-ray imaging platforms not only provide high-resolution anatomical images but also incorporate advanced features such as real-time imaging. These capabilities are pivotal for monitoring tumor response, dynamically adjusting treatment parameters, and ensuring precise delivery of radiation during therapy.

This chapter discusses the various components of x-ray imaging systems designed for radiotherapy, detailing their interactions with biological tissues and the core principles that ensure accurate tumor localization and effective treatment delivery. Additionally, it explores imaging concepts, techniques in dual-energy (DE) imaging, and their role in enhancing radiotherapy applications.

1.1 X-ray Generation

1.1.1 X-ray Tube

The x-ray tube (Figure 1.1) is the core component of x-ray imaging systems, necessary for generating the x-rays needed in both medical diagnostics and image guided radiation therapy. An x-ray tube consists of a vacuum-sealed enclosure housing a cathode and anode, which are essential for the emission and acceleration of high-energy electrons. The cathode, typically made from tungsten due to its high heat tolerance and efficient electron emission, utilizes thermionic emission to release electrons in vacuum when a voltage is applied. These electrons are accelerated towards the anode by the high electrical potential difference across the tube. The anode, also composed of tungsten to withstand thermal stress and electron impact, features an angled target to dissipate heat and control the direction of the x-ray beam.[1]

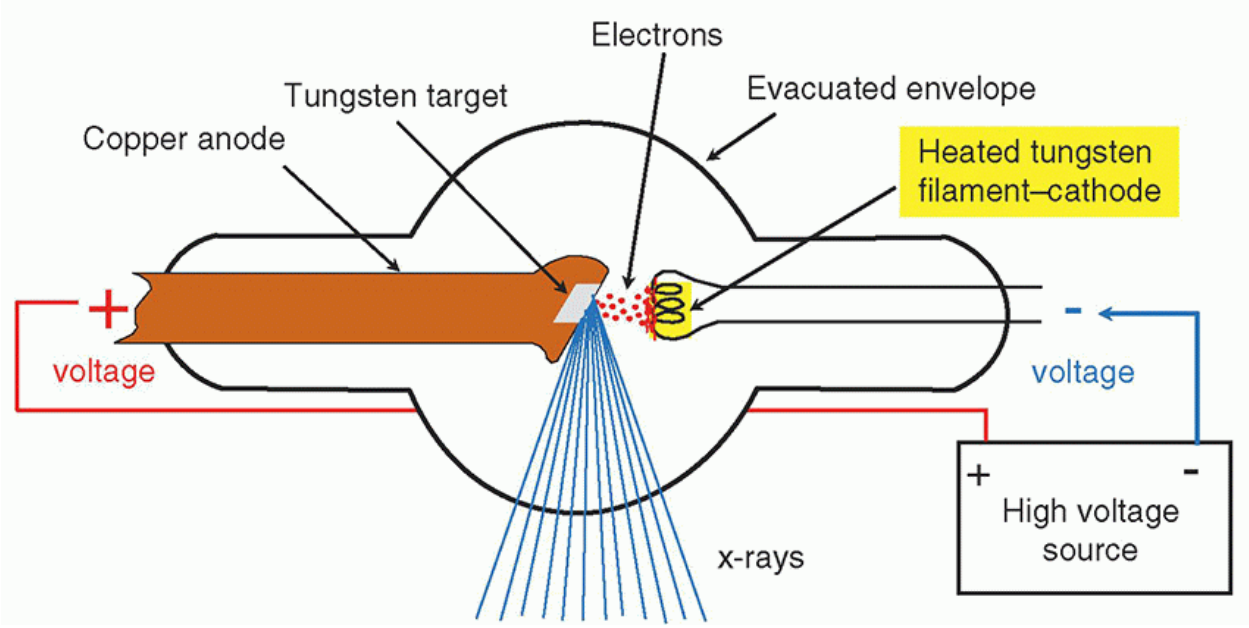

Figure 1.1: A basic x-ray tube demonstrating its components and the production of x-rays.[1]

Critical parameters for operating the x-ray tube include tube current (mA), tube voltage (kVp), and exposure time (s). Tube current controls the electron flow from the cathode to the anode, thereby influencing the intensity of the x-ray beam. Tube voltage determines the energy level of the emitted x-rays, affecting their penetration depth and contrast resolution in clinical imaging. The voltage directly affects the maximum photon energy emitted by the x-ray tube,

while the average energy is usually about one third the maximum. Exposure time regulates the duration of x-ray emission. The product of tube current and exposure time, expressed as milliampere-seconds (mAs), is a commonly used method to describe the x-ray tube's output.

1.1.2 Bremsstrahlung Radiation

The primary mechanism of x-ray production within the tube is bremsstrahlung radiation, which occurs when high-speed electrons decelerate upon approaching the tungsten atoms in the anode. This rapid deceleration results in the conversion of kinetic energy into electromagnetic radiation, predominantly in the form of x-rays. However, only about 1% of the electron's kinetic energy is converted into usable x-ray photons, with the remaining 99% dissipated as heat. This high level of heat generation necessitates a rotating anode and the use of materials with high melting points, such as tungsten, to ensure the durability and performance of the x-ray tube.

The production of bremsstrahlung x-rays per atom is proportional to Z^2/m^2, where Z is the atomic number of the material and m is the mass of the incident particle. The bremsstrahlung radiation within the x-ray tube manifests as a continuous spectrum of x-ray energies, directly influenced by the kinetic energy of incident electrons and the atomic number of the anode material.

The efficiency of bremsstrahlung radiation highlights the importance of optimizing tube design and operational parameters to achieve diagnostic quality while minimizing heat accumulation. Unfiltered bremsstrahlung spectra exhibit an inverse relationship between photon energy and intensity, while filtered spectra have their low-energy photons attenuated, allowing for most photons to be within the diagnostic range (Figure 1.2).

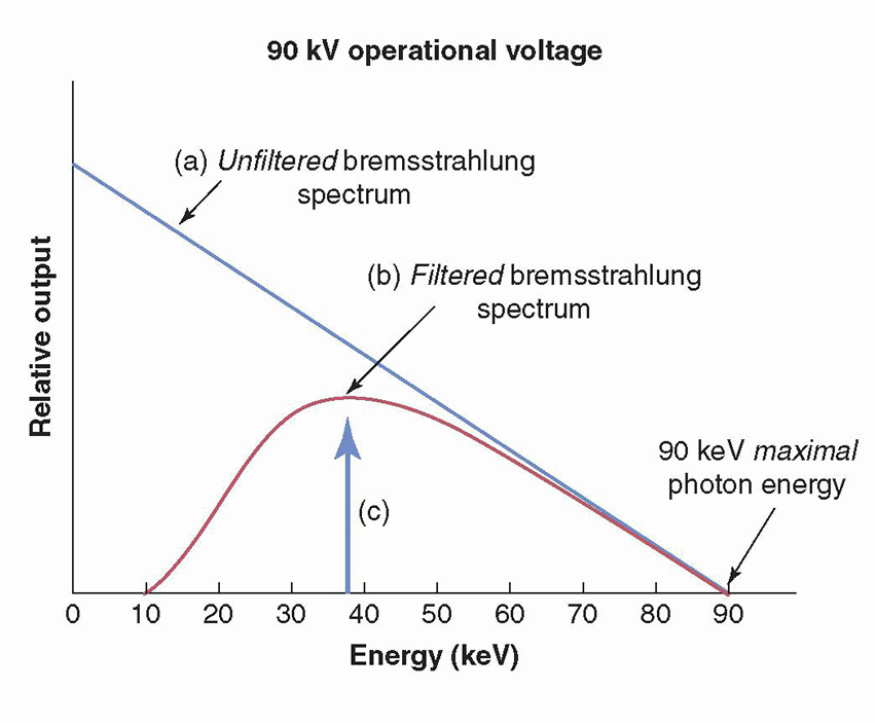

Figure 1.2: Demonstrating the necessity of filters to attenuate low-energy photons outside the diagnostic energy range. [1]

1.1.3 X-ray Output

X-ray tube parameters have varying effects on the photon output. Increasing the mAs of the tube results in a directly proportional, linear increase of photons produced. Increasing the tube potential results in a quadratic increase. Finally, increasing the cathode filament current has an exponentially larger effect on the output. Because of its severe effect on photon production, filament current is left out from imaging techniques, and only the former two along with exposure time are tuned as parameters. Figure 1.3 demonstrates these relations.

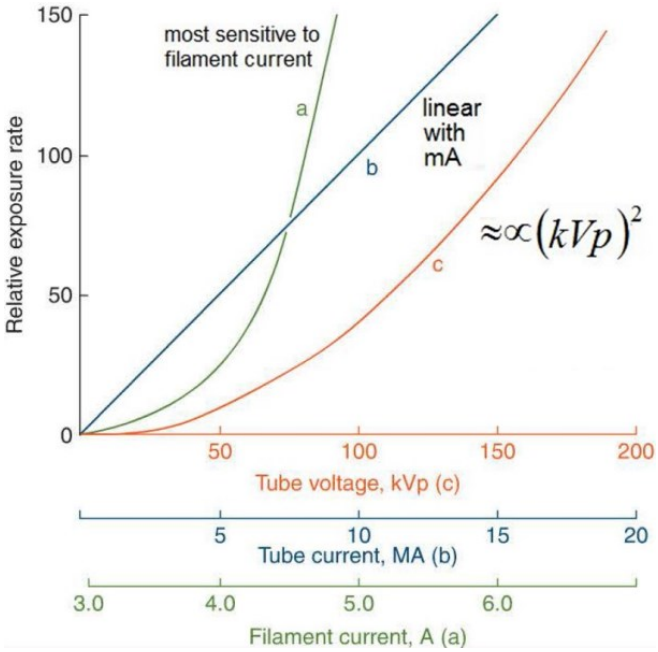

Figure 1.3: X-ray tube parameters and their effect on photon output. [1]

1.2 X-ray Interactions with Matter

X-rays generated via bremsstrahlung within the tube interact with biological tissues primarily through absorption, scattering, or transmission mechanisms. Absorption occurs when x-ray photons transfer their energy to atomic electrons within tissues, causing ionization or excitation. This process depends on the energy of the incident photon and the atomic number (Z) of the material. Tissues with higher atomic numbers, such as bone ($Z \approx 12$)[1], exhibit greater absorption rates, making them more radiopaque compared to softer tissues ($Z \approx 7$)[1]. Transmission occurs when x-ray photons pass through tissues without interaction, contributing to the formation of x-ray images.

Photon interactions (Figure 1.4) include Rayleigh scattering, where x-ray photons interact coherently with bound electrons within tissues without energy transfer, more prevalent at lower energies but with minimal impact on diagnostic image contrast due to attenuation by the tube window and housing[1]. Compton scattering, predominant at diagnostic x-ray energies, occurs when an incident photon collides with a loosely bound (free) electron, redirecting the photon and ejecting the electron. This type of scattering is independent of tissue atomic number (Eq. 1.1) but is instead influenced by the electron density ρ of the material, which correlates

with its physical density.

$$\frac{\mu_C}{\rho} \propto \frac{Z^0}{h\nu^{0.5\to1}} \tag{1.1}$$

In soft tissues (Z ≈ 7), Compton scattering becomes more prevalent than photoelectric absorption at energies above[2] approximately 25 keV. In contrast, due to bone's higher atomic number (Z ≈ 12), Compton interactions only surpass photoelectric interactions at energies exceeding[2] around 40 keV.

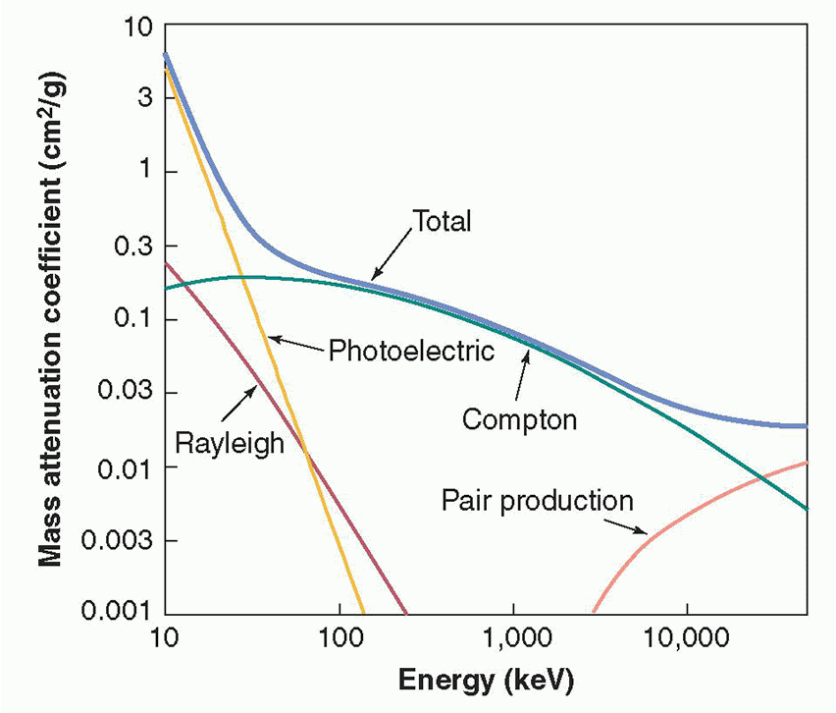

Figure 1.4: Mass attenuation coefficients for soft tissue (Z ≈ 7) as a function of photon energy. [1]

Photoelectric absorption, prevalent at lower x-ray energies, occurs when photons transfer all their energy to inner-shell electrons, ejecting them from their orbitals. This process strongly depends on tissue atomic number and photon energy (Eq. 1.2). Pair production, requiring very high photon energies (>1.02 MeV), creates an electron-positron pair near a nucleus but is irrelevant for diagnostic imaging due to its high energies.

$$\frac{\mu_{PE}}{\rho} \propto \left(\frac{Z}{h\nu}\right)^3 \tag{1.2}$$

Energy-dependent attenuation of x-rays through biological tissues varies with photon energy and tissue composition, particularly near k-edge energies where sharp increases in attenuation occur corresponding to electron binding energies. Figure 1.5 shows the variation of linear attenuation coefficients across different tissue types with varying energies, as well as blood injected with an iodine (Z = 53) contrast agent. Also visible are absorption edges for the higher Z materials.

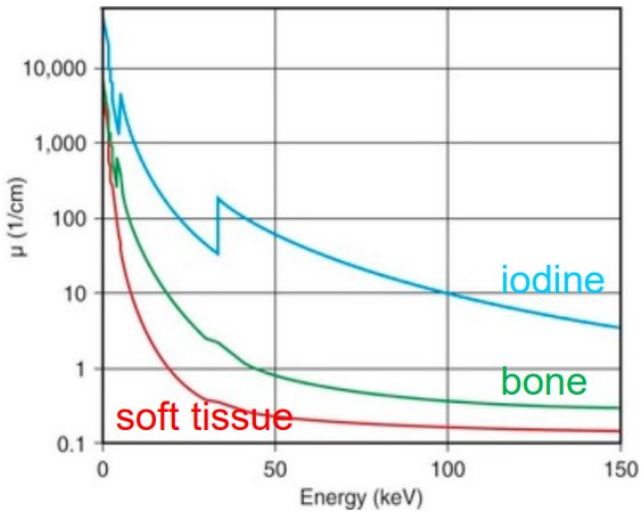

Figure 1.5: Photoelectric linear attenuation coefficients for soft tissue, bone and iodine. [1]

A photon cannot undergo photoelectric interaction if its energy is less than the binding energy of the atomic shell it encounters, leading to a sharp decrease in the probability of photoelectric absorption just below this binding energy. The energy at which this decrease occurs is called an absorption edge and is designated by a letter for the atomic shell (e.g., K, L, M, …). The absorption edge energy increases with the atomic number (Z) of the element. For instance, soft tissue elements have absorption edges in the lower energy range, while iodine, used in contrast agents, and tungsten, used in x-ray tubes, have higher absorption edges.[1]

In most instances, entirely pure elements in the patient's body are not being dealt with. Instead, complex compositions of molecules and biological materials are involved. This necessitates the effective atomic number Z_{eff}, which is described by the following equation[3]:

$$Z_{eff} = \left(\sum a_i Z_i^{2.94}\right)^{\frac{1}{2.94}}, \tag{1.3}$$

where all elements of the mixture are summed together, and a_i is the fractional contribution to the total number of electrons. Because of its high Z dependence, this equation is defined for the photoelectric effect. Table 1.1 shows a collection of commonly imaged materials in the body, and their densities and effective atomic numbers in comparison with air and water.

Table 1.1: Densities and effective atomic numbers of common materials in x-ray imaging. [3]

Material	ρ (g/cm^3)	Z_{eff}
Water	1	7.5
Muscle	1.04	7.6
Fat	0.92	6.5
Air	0.001	7.8
Lung (inhale)	0.26	7.6
Bone	1.65	12.3

As will be covered in Section 1.4, photon interactions in materials of different densities and atomic numbers strongly influence the visibility of an object. For instance, as demonstrated in Fig. 1.6, a lung should be expected to appear as black in an x-ray because of the incredibly low density of air, while the ribs should appear as white since bone has relatively high density and atomic number.

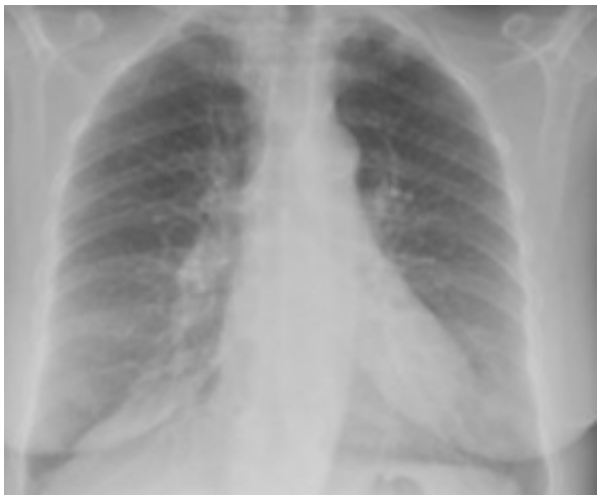

Figure 1.6: A typical chest x-ray. Being mostly air, the lungs appear black from the detector receiving more signal, while the bones of the chest and spine, and soft tissue such as the heart appear white.

1.3 X-ray Detection

X-ray imaging systems also include detectors, which capture photons after they pass through the patient to create diagnostic images. Historically, imaging systems utilized screen-film techniques. Contemporary approaches predominantly employ digital methods, with flat panel detectors (FPDs) being a common choice. FPDs typically feature arrays of thin-film transistor (TFT) dexels (detector elements), each capable of converting incident x-ray photons into electrical signals for digital processing[1]

These detectors employ either direct or indirect conversion methods, each influencing spatial resolution and image quality differently. Indirect FPDs incorporate scintillators such as CsI or Gd_2O_2S, positioned in front of the TFT array. X-rays interacting with the scintillator produce light photons, which subsequently activate a photodiode to generate an electrical charge (Figure 1.7A).[1]

Conversely, direct conversion FPDs use semiconductor materials like amorphous selenium (a-Se), within which x-rays directly produce electron-ion pairs. This method minimizes lateral spread, resulting in improved spatial resolution by concentrating signal collection within individual dexels (Figure 1.7B).[1]

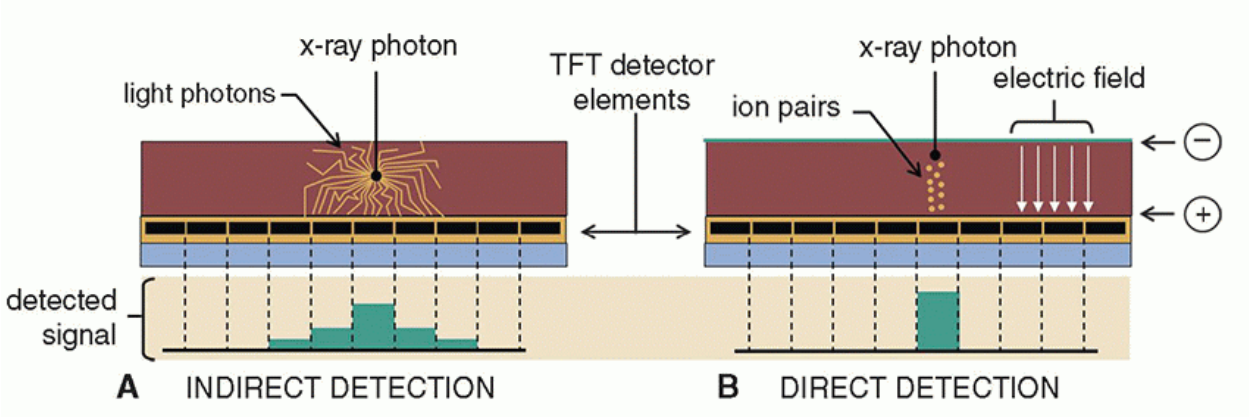

Figure 1.7: Indirect and direct TFT-based x-ray detectors using a scintillator (A) or a semiconductor (B). [1]

Beyond FPDs, x-ray imaging systems encompass other detectors such as computed radiography (CR) systems and image intensifiers (IIs), each tailored to specific clinical needs. CR systems employ photostimulable phosphor plates to temporarily store x-rays and release them as visible light upon stimulation, suitable for high-throughput imaging scenarios.[1] IIs amplify weak x-ray signals through electron multiplication before conversion to digital format, a necessary feature for real-time fluoroscopy and interventional procedures. The performance of these detectors, characterized by spatial resolution, contrast sensitivity, and dynamic range, plays a critical role in achieving precise diagnosis and image guided radiotherapy.[1]

1.4 Image Quality in X-ray Imaging

Achieving high-quality x-ray images is highly important for accurate diagnosis and image guided radiotherapy. This involves optimizing several key factors: noise management, contrast enhancement, and spatial resolution.

1.4.1 Noise

Noise in x-ray imaging poses a significant challenge by introducing random fluctuations in image intensity that can obscure critical diagnostic information. It arises from multiple sources, including electronic components, photon interactions within the detector, and environmental factors. Effective noise reduction techniques are necessary to enhance image quality.[1]

Quantum noise, directly linked to the output of the x-ray tube, stems from the finite number of photons interacting within the detector. The severity of quantum noise σ is proportional to the square root of the incident photon count per pixel N, following Poisson statistics:

$$\sigma = \sqrt{N} \tag{1.4}$$

The relative noise level quantifies the strength of the signal against noise interference:

$$relative\ noise = \frac{\sigma}{N} = \frac{1}{\sqrt{N}} \tag{1.5}$$

The inverse of the relative noise level may also be expressed as the signal-to-noise ratio (SNR), quantifying the strength of the signal against noise interference:

$$SNR = \frac{N}{\sigma} = \sqrt{N} \tag{1.6}$$

Increasing the number of incident photons through adjustments in mAs or kVp values can effectively reduce quantum noise.

Anatomical noise presents another challenge, arising from patient anatomy that overlaps with regions of diagnostic interest. An example of this, as will be seen later in this thesis, is how the lung tumors may be overlapped by rib structures, limiting diagnostic clarity.

1.4.2 Contrast

Contrast is a critical aspect of x-ray imaging, enabling the differentiation of various tissues or structures within an image based on their average grayscales. Techniques like dual-energy imaging (discussed later) leverage these differences in tissue composition to enhance contrast and thereby improve diagnostic accuracy.

Because the photoelectric effect dominates at lower diagnostic energies while Compton scattering becomes more prevalent at higher energies, mass attenuation coefficients of materials decrease rapidly at lower energies and more gradually at higher energies. This shift in dominance leads to reduced contrast between different tissues at higher energies. Demonstrating the effect of energy on contrast, Figure 1.8 shows a lung phantom with a tumor model in high

(140 kVp) and low (60 kVp) energy scenarios. The high energy image shows a smaller differentiation between rib bones and surrounding soft tissue compared to the low energy image due to the increased influence of Compton scattering.

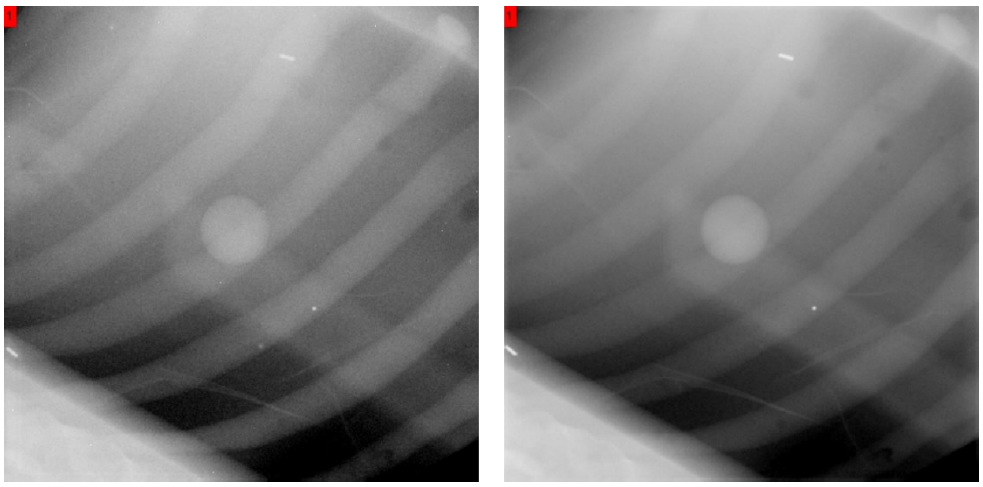

Figure 1.8: (Left) Low energy, 60 kVp, and (Right) high energy, 140 kVp, images of a spherical tumor model in an anthropomorphic lung phantom.

Subject contrast reflects the difference in x-ray intensity passing through a lesion compared to adjacent tissues. It primarily depends on the differential attenuation characteristics of tissues within the patient, unaffected by detector properties. Lower x-ray energies tend to yield higher subject contrast due to smaller difference in attenuation coefficients between the object and the background (see Fig. 1.5), particularly in tissues with higher atomic numbers.[1]

$$C_s = \frac{\bar{q}_A - \bar{q}_B}{\bar{q}_B} \tag{1.7}$$

Here, $\bar{q}_A$ and $\bar{q}_B$ reflect photon fluence levels after having travelled through the patient, incident on the detector. This cannot be measured directly, as additional contrast will be lost due to the detector. Detector contrast will vary depending on the detector type (nonlinear response with screen-film radiography vs. linear response with digital x-ray detectors).[1]

The contrast-to-noise ratio (CNR) is another key metric used to assess image quality, accounting for both contrast and the impact of noise. It is calculated as:

$$CNR = \frac{\left|\bar{x}_q - \bar{x}_{bkg}\right|}{\sigma_{bkg}} \tag{1.8}$$

where $\bar{x}_q$ is the average signal in a region of interest (ROI) containing the lesion, $\bar{x}_{bkg}$ is the average signal in a background ROI, and σ_{bkg} is the standard deviation of the signal in the background ROI. CNR provides a relative measure of how well the signal (contrast) stands out against background noise, essential for optimizing imaging parameters to enhance tumor visibility.

1.4.3 Spatial Resolution

Spatial resolution refers to the ability of an imaging system to discern small structures or details within an image. It is influenced by factors such as detector pixel size, light blurring (light scatter), and focal spot blurring which depend on geometric magnification. High spatial resolution can be useful for accurately visualizing anatomical features and enabling the precise localization of tumor boundaries.[1]

1.4.4 The Rose Model and Rose Criterion

Albert Rose defined "signal" as a change in the number of quanta of an object, integrated over the area (A) of the object. This results in a modified version of the SNR formula[1], shown by Eq. 1.9.

$$SNR = \frac{A(\bar{q}_b - \bar{q}_0)}{\sqrt{A\bar{q}_b}} \tag{1.9}$$

Using this definition of SNR allows for the use of the Rose model, which quantifies the detectability of signals against background noise in imaging systems. Rose established that an SNR ≥ 5 typically ensures object detectability, but detection performance decreases as SNR approaches zero. This is known as the Rose Criterion. However, this criterion does not consider noise texture variations, which can significantly affect visibility[1]. Rose Criterion works under "Rose conditions", i.e., uniform object in a uniform background with the assumption of uncorrelated Poisson noise. The x-ray incident on the detector is Poisson, but due to the loss of spatial resolution in the detector, the imaging signal is correlated and not Poisson.

1.5 Dual-energy X-ray Imaging

Dual-energy X-ray imaging (DE) techniques enhance diagnostic imaging by improving the quality of radiographs and reducing anatomical noise, thus improving tumor visualization[3,4].

DE imaging involves acquiring low energy (LE) and high energy (HE) images and combining them to cancel out specific tissue types. Figure 1.9 shows spectra of low and high kVp x-ray tube outputs.

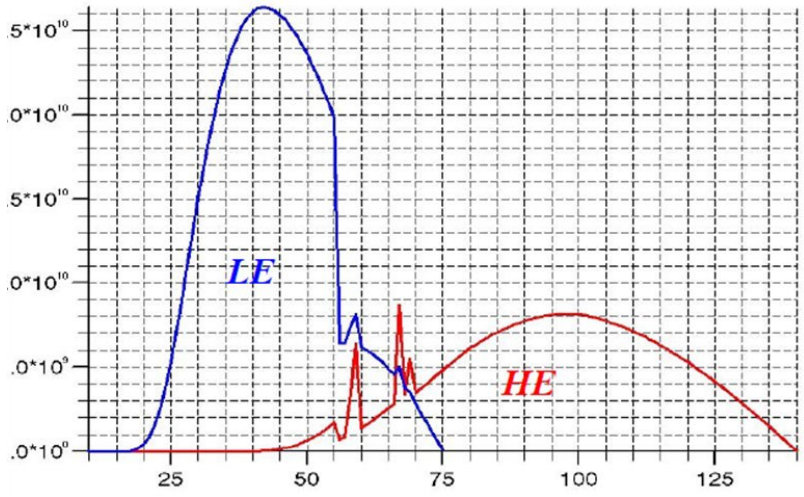

Figure 1.9: Photon energy spectrum of low and high energy x-ray outputs. [5]

1.5.1 Weighted Logarithmic Subtraction

Weighted logarithmic subtraction is a foundational DE imaging technique. It leverages images obtained at two distinct energy levels: LE and HE, and enhances tissue contrast and material differentiation using the logarithmic subtraction formula:

$$\log(DE) = \log(HE) - \omega \cdot \log(LE) \qquad (1.10)$$

In this formula, ω is a weighting factor that adjusts the contribution of the high-energy image to optimize contrast resolution and material differentiation. The technique uses Beer's Law to describe x-ray attenuation through bone and soft tissue. The logarithm of the initial x-ray intensity for both LE and HE beams is taken, and then the LE and HE images are subtracted, introducing a weighting factor for tissue. For example, a soft-tissue-only DE image (with bone suppression) is created by selecting an appropriate weighting factor to cancel bone. Conversely, to create a bone-only DE image, the HE image is subtracted from the LE image, using a weighting factor to cancel soft tissue (Eq. 1.10).

The selection of the weighting factor is crucial. Theoretically, it can be derived to cancel

bone by setting bone-related terms to zero in the logarithmic equation. Similarly, a weighting factor for canceling soft tissue can be calculated. However, the constant weighting factors used in this technique may lead to incomplete suppression of specific tissues of varying thicknesses across the image due to beam hardening effects, where LE and HE beams experience different attenuation in regions of non-uniform tissue thickness. As a consequence of this, later in this thesis, DE weighting factors are instead chosen manually via an algorithm that minimizes contrast between ROIs on the rib bone and background in proximity to the tumor.

The following is a derivation of the weighted logarithmic subtraction equation. Assuming that a high energy (HE) and low energy (LE) beam both pass through soft tissue and bone of thickness T and B, respectively (Fig. 1.10), both beam intensities will be attenuated by the material, according to the Lambert-Beer law. Tissue and bone have mass attenuation coefficients of μ^t and μ^b respectively.

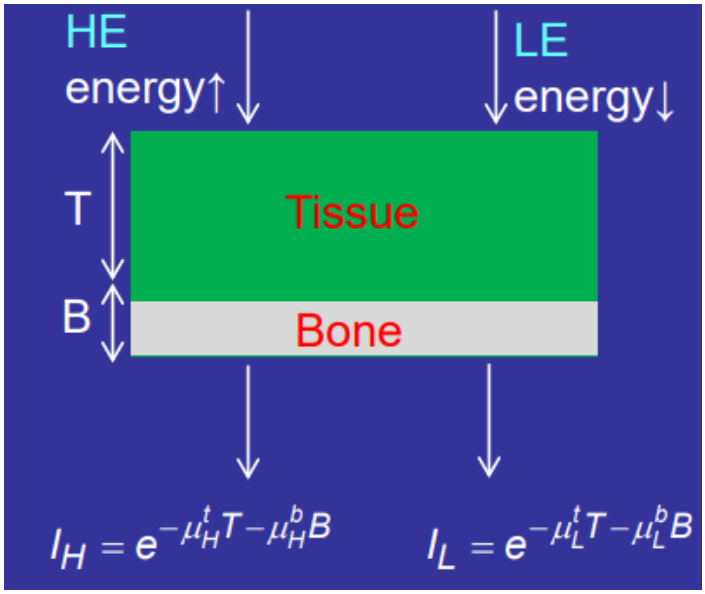

Figure 1.10: High and low energy photon beams and their attenuated intensities.

Taking the logarithm of both high and low energy intensities:

$$\log(I_H) = -\mu_H^t T - \mu_H^b B \tag{1.11}$$

$$\log(I_L) = -\mu_L^t T - \mu_L^b B \tag{1.12}$$

By applying the form of the weighted subtraction equation (Eq. 1.10), weighting factors for the respective tissue types can be determined. Here, T_{im} and B_{im} are dual energy weighted subtracted

images only showing soft tissue or bone respectively:

$$T_{im} = \log(I_H) - \omega_t \log(I_L) = \left[-\mu_H^t + \frac{\mu_H^b}{\mu_L^b}\mu_L^t\right]T \tag{1.13}$$

$$B_{im} = -\log(I_H) + \omega_b \log(I_L) = \left[\mu_H^b - \frac{\mu_H^t}{\mu_L^t}\mu_L^b\right]B \tag{1.14}$$

$$\omega_t = \frac{\mu_H^b}{\mu_L^b} \tag{1.15}$$

$$\omega_b = \frac{\mu_H^t}{\mu_L^t} \tag{1.16}$$

The values for ω and μ must be determined empirically, because these equations assume monoenergetic photons. As shown previously in Fig. 1.9, x-rays are produced as a spectrum of energies.

1.5.2 Bone Suppression in Dual-energy Imaging

Bone suppression techniques in dual-energy imaging capitalize on the higher attenuation of bone at higher X-ray energies compared to soft tissues. By emphasizing soft tissue details and minimizing bone in the resultant image, this technique enhances the clarity of structures like lung tumors. Figure 1.11 illustrates this process.

Figure 1.11: Example of bone suppression in dual-energy imaging.

By adjusting the value of ω in equation 1.10 from the previous section, a large range of dual energy images can be produced. Figure 1.12 shows the effects of ω on bone suppression. For the scenario of a tumor model in an anthropomorphic lung phantom, the ideal weighting

factor is 0.75 (center image). The left image has a lower value of 0.40, resulting in more contribution from the high energy component. The right image has a higher value of 1.00, causing the surrounding rib bones to start appearing as negative space (over-suppression of bone signal).

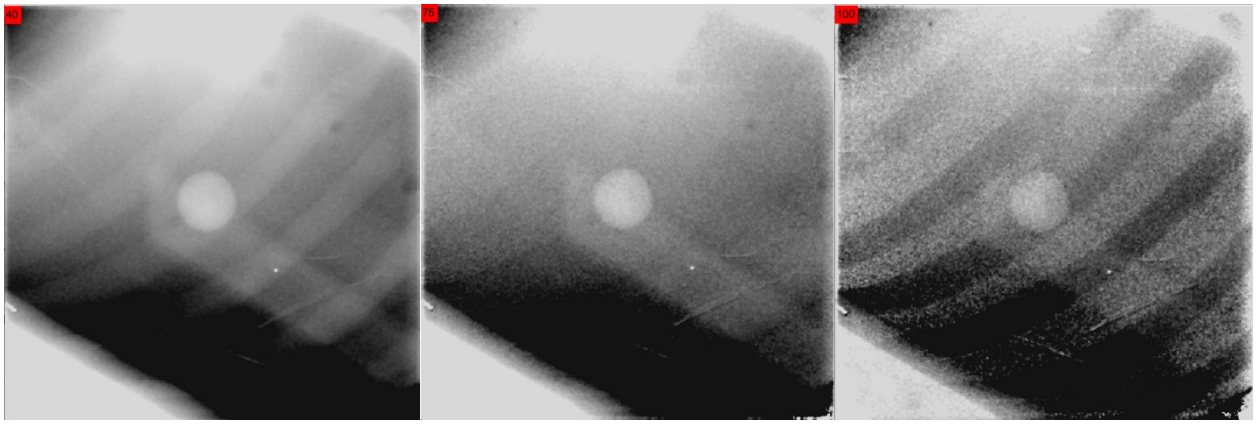

Figure 1.12: Dual energy images with varying weighting factors. From left to right: 0.40, 0.75, 1.00.

1.5.3 Dual-Energy Imaging Techniques

Various techniques for DE imaging are currently implemented clinically. Some of these techniques are described below in the context of dual energy computed tomography (CT). Unless where specifically pointed out, these techniques also apply to projection dual energy imaging.

Single exposure DE imaging (Fig. 1.13) achieves simultaneous acquisition of low-energy (LE) and high-energy (HE) images during a single x-ray exposure[4,6]. This method uses two detector plates, with a copper filter between them to harden the beam by filtering out low-energy photons. The first detector produces the LE image, and the hardened beam that passes through the filter generates the HE image on the second detector. This approach effectively eliminates patient motion artifacts that can occur between separate LE and HE exposures. However, it tends to have a lower signal-to-noise ratio (SNR) due to the attenuation of photons by the first detector and copper filter, leading to reduced signal and increased noise in the HE image[6]. Moreover, large spectra separation cannot be achieved since both HE and LE images have the same kVp.

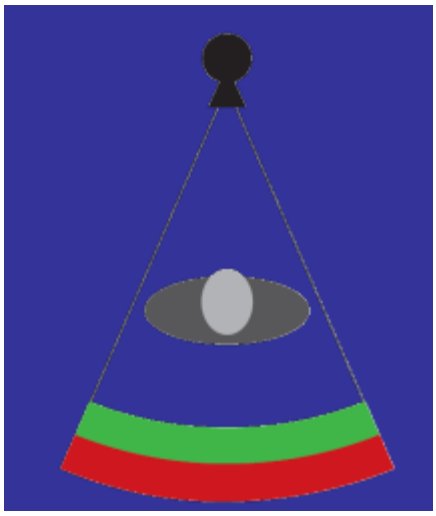

Figure 1.13: Single exposure DE technique. Two detector plates (green and red) are used.

Double Exposure DE imaging involves sequentially acquiring LE and HE images using different kVp settings[7], often with additional filters to enhance spectral separation. This technique improves SNR compared to single exposure methods but can introduce misregistration artifacts due to patient motion between exposures. Despite the short acquisition time between images, motion artifacts can still occur, especially in cases involving cardiac motion, potentially leading to inaccuracies in detecting smaller structures[8,9].

Single source DE imaging (Fig. 1.14) uses one x-ray source that rapidly alternates on the order of milliseconds between LE and HE settings, having applications in radiography as well as CT. This method ensures good temporal registration between LE and HE images but may experience reduced dose efficiency, as the tube parameters (mAs) for LE and HE beams cannot be modified separately[10,11].

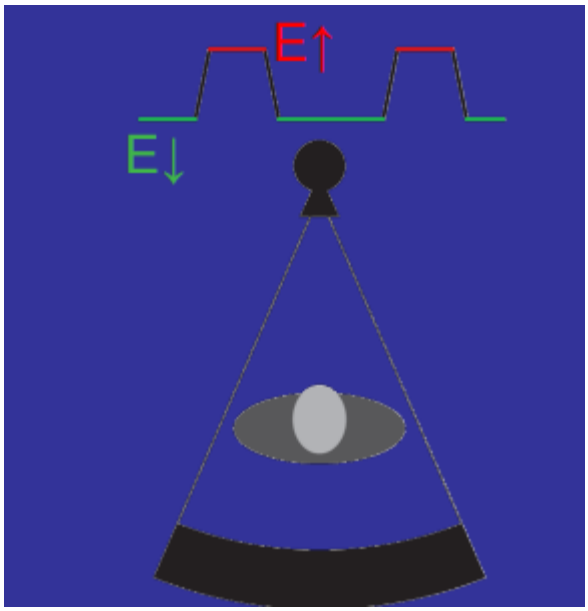

Figure 1.14: Single source DE imaging technique with a rapidly alternating kVp switch.

Double source DE imaging (Fig. 1.15) employs two x-ray sources and two detector arrays positioned at a 90° offset, acquiring LE and HE images simultaneously. This technique, which is specific to CT, enhances imaging speed and accuracy, reduces motion artifacts, and allows for better mAs and beam filtration optimization. However, the projection data are acquired in a double-helix geometry, which can complicate DE image generation due to non-coincident LE and HE projections[12]. Additionally, cross-scatter radiation between the detectors must be corrected for accurate imaging[13].

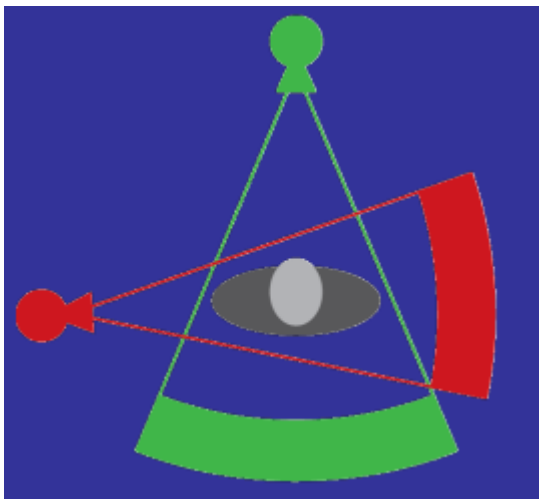

Figure 1.15: Dual source DE imaging whose HE and LE sources/detectors are orthogonal to one another.

1.5.4 Noise Reduction Algorithms

While dual-energy (DE) imaging excels at reducing anatomical noise and enhancing lesion visualization, it has the drawback of amplifying quantum noise. Logarithmic subtraction can exacerbate noise due to noise propagation[14], and to address this, various noise reduction algorithms have been developed.

One such technique is the anti-correlated noise reduction (ACNR) algorithm[14,15]. This method uses a high-pass filter h_{HPF} on a bone-only DE image I_{DE}^{B}, isolating quantum noise and residual edge artifacts (Equation 1.17). The filtered noise image is then added to the soft-tissue-only DE image I_{DE}^{ST} with a noise suppression weighting factor ω_n to give a noise-reduced DE image $I_{DE,ACNR}$, effectively reducing noise by leveraging the anti-correlation[15] of noise between soft-tissue-only and bone-only images. This approach significantly improves image quality by minimizing noise while preserving important anatomical details.

$$\log\left(I_{DE,ACNR}\right) = \log(I_{DE}^{ST}) + \omega_n \log(I_{DE}^{B}) * h_{HPF} \tag{1.17}$$

Figure 1.16 shows the ACNR algorithm being applied to a lung tumor in a lung phantom. A complementary bone only image is created by adjusting ω in the weighting logarithmic subtraction, applying a high-pass filter and weighting factor ω_n to the complementary image, then adding the new image back to the original soft-tissue only image. This resulting noise-reduced DE image may then be processed easier by analysis techniques such as template matching described in the next chapter.

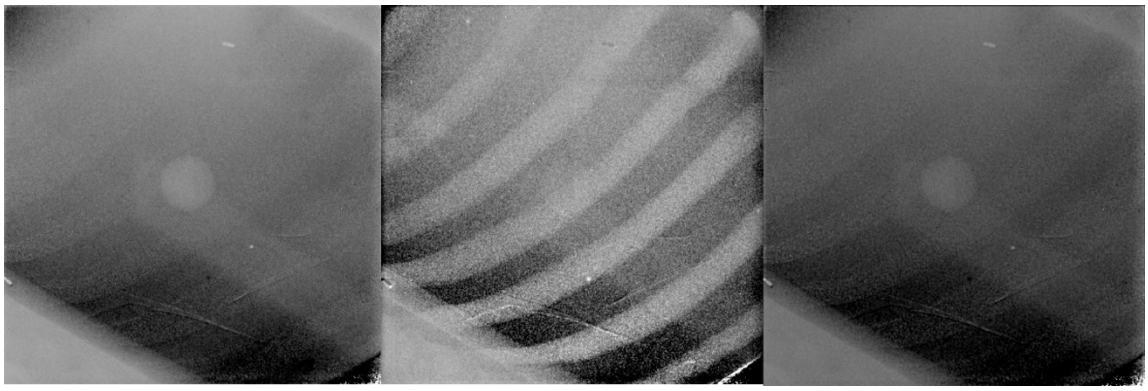

Figure 1.16: ACNR algorithm is applied to the weighted logarithmic subtracted image (left) by creating a complementary bone-only image (middle) to create a noise-reduced DE image (right).

1.6 Radiotherapy

Radiotherapy is crucial in treating cancer, especially lung cancer, which presents significant global health challenges due to its high incidence and mortality rates. Advancements in imaging technologies have greatly enhanced the precision of radiotherapy, enabling more accurate targeting of tumors while minimizing damage to surrounding healthy tissues. This section explores the fundamental aspects of radiotherapy, focusing on its integration with advanced imaging techniques. Using MV photons from a linear accelerator (linac), radiation therapy (RT) effectively targets malignancies by delivering a uniform dose to the tumor volume while sparing nearby healthy tissues. Stereotactic body radiation therapy (SBRT), for instance, delivers a concentrated radiation dose over a few treatments, such as 12 Gy in 4 fractions totaling 48 Gy, showing promise in treating metastatic lung tumors[16]. The success of SBRT hinges on precise delivery facilitated by image-guided radiation therapy (IGRT), which uses in-room imaging techniques such as cone-beam CT (CBCT) to align patients accurately. While CBCT provides detailed volumetric images, projection room mounted x-ray imaging systems may also have certain advantages for image guidance. Alignment is achieved by volumetrically matching the acquired CBCT images to the planning CT or matching the acquired projection images to digitally reconstructed radiographs (DRRs) created from the planning CT.

1.6.1 CT Simulation and DRRs

During CT simulation, patients are positioned on a CT scanner in the same manner they will be positioned during treatment. The resulting images enable clinicians to delineate the tumor boundaries, known as the Gross Tumor Volume (GTV), and identify critical structures that must be avoided or given lower doses of radiation. DRRs, as exemplified by Figure 1.17, are synthesized from CT simulation data to simulate the treatment setup and aid in patient positioning. DRRs provide a visual representation of how the x-ray images would appear during the actual treatment sessions, helping to verify patient positioning and ensuring the alignment of treatment fields.[17]

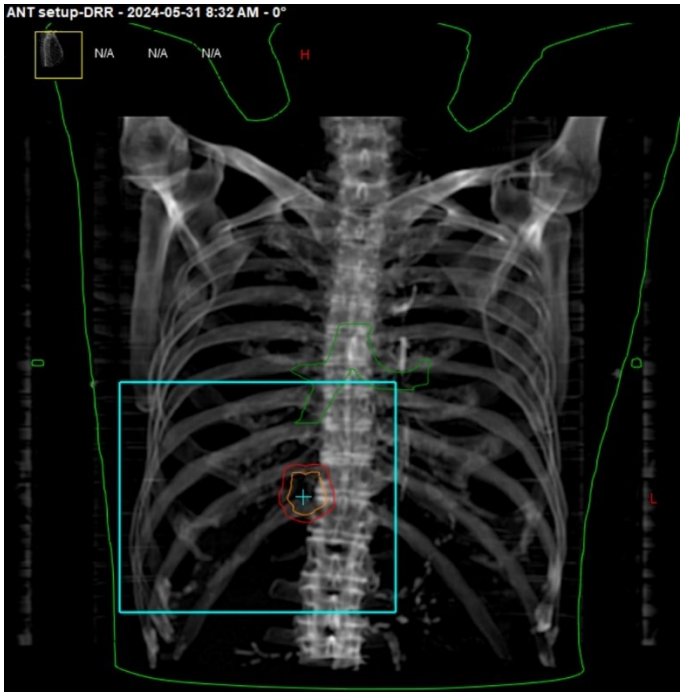

Figure 1.17: A digital reconstructed radiograph (DRR) of a patient's torso.

1.6.2 Treatment Planning and Workflow

Radiotherapy planning involves defining several critical volumes to ensure accurate dose delivery. The Gross Tumor Volume (GTV) is the visible extent of the malignant tumor based on imaging studies. The Clinical Target Volume (CTV) includes the GTV, and any areas suspected of containing microscopic disease, accounting for potential subclinical spread. The Planning Target Volume (PTV) is the CTV plus an additional margin to account for variations in treatment delivery, patient movement, and setup errors. This margin ensures that the prescribed dose is delivered to the entire CTV despite these uncertainties. The Internal Target Volume (ITV), specifically for tumors subject to movement (e.g., lung tumors), encompasses the CTV and accounts for internal physiological movements, particularly respiratory motion, captured through techniques like 4DCT.

The radiotherapy process typically follows a structured workflow. CT Simulation (CT Sim) involves initial imaging to create a volumetric image of the patient's anatomy in the treatment position (Fig. 1.18). Treatment Planning utilizes specialized software like Eclipse, where clinicians design a radiation treatment plan that defines the optimal radiation dose

distribution. This involves configuring treatment fields to ensure maximum tumor coverage and minimal exposure to healthy tissue. Pre-treatment verification uses cone beam CT (CBCT) or other imaging modalities immediately before each treatment session to verify patient positioning and ensure alignment with the treatment plan (Fig. 1.19).

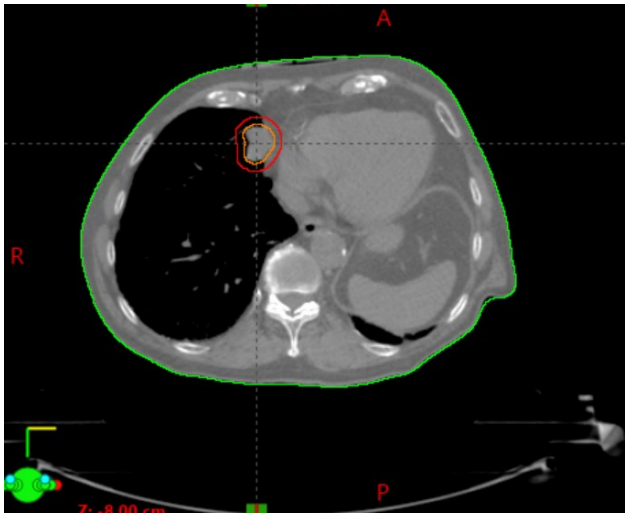

Figure 1.18: An axial view of planning CT for a lung patient. Outlined are the GTV and PTV of the tumor.

Figure 1.19: A CBCT of the same lung patient as Figure 1.18 immediately prior to treatment. The image is lower quality due to increased scatter caused by the larger irradiation volume of the cone beam.

1.6.3 Techniques to Manage Tumor Motion

Lung tumors pose a unique challenge due to their movement with respiration[18–20]. Techniques to manage this include 4DCT Imaging[21], which captures the tumor motion over the respiratory cycle, providing a comprehensive view of its movement. This data informs the creation of the ITV. Gating[22] synchronizes radiation delivery with specific phases of the breathing cycle to target the tumor when it is in a consistent position. Breath-hold techniques[23] require patients to hold their breath during treatment to stabilize the tumor's position, reducing motion-related uncertainties. Real-time Tumor Tracking (RTTT) involves advanced systems that continuously monitor and adjust for tumor movement during treatment, ensuring precise dose delivery. The benefits of RTTT include shorter treatment time, and less patient discomfort. Additionally, the usage of markerless tumor tracking[24–29] allows for the omission of internal fiducials and external motion surrogates[30,31], leading to more accurate tumor localizations and the prevention of pneumonitis or pneumothorax in the patient[32,33]. Figure 1.20 shows a visualization of three motion management methods.

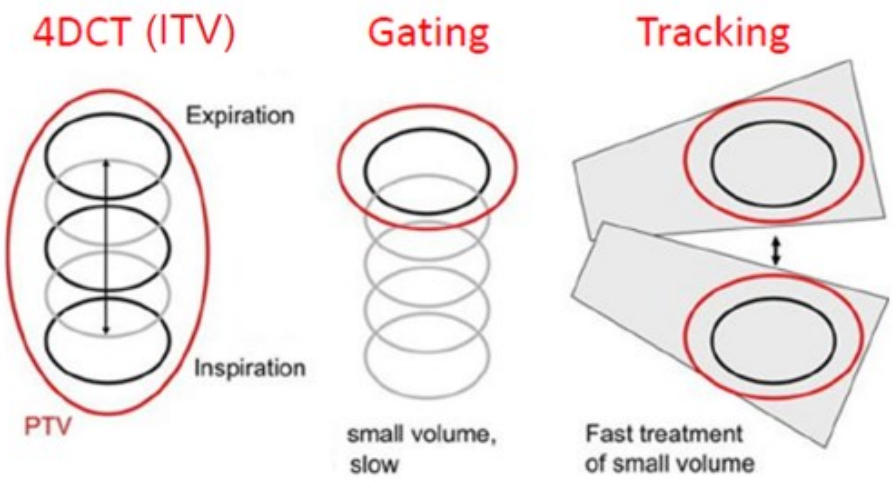

Figure 1.20: Various methods of tumor motion management.[34]

1.6.4 Applications of Dual-Energy Imaging in Radiotherapy

Dual-energy (DE) imaging offers multiple approaches to enhance radiotherapy through improving treatment precision and optimizing dose delivery. This section explores current applications of DE imaging techniques, as detailed across comprehensive studies[35,36].

DE imaging, particularly in Dual-Energy CT (DECT) and Dual-Energy Cone Beam CT (DE-CBCT), stands at the forefront of medical imaging advancements. By acquiring images at multiple energy levels, DE imaging enhances soft tissue contrast and mitigates artifacts such as beam hardening and metal implants[37–39]. These capabilities are critical for precise tumor delineation and localization, essential in complex radiotherapy procedures like Stereotactic Body Radiation Therapy (SBRT) and stereotactic radiosurgery (SRS)[37].

In CBCT, DE imaging significantly improves image quality by reducing artifacts common in conventional CBCT, particularly beneficial in cases involving metallic implants or bony structures[40–44]. Enhanced tumor visualization and delineation are important for precise treatment delivery, particularly in SBRT. DECT enhances lesion conspicuity and tumor boundary delineation, thereby refining treatment planning and delivery accuracy[37].

Accurate dose calculation is paramount in external beam radiation therapy to optimize treatment outcomes and minimize risks to healthy tissues. DE-CBCT facilitates precise estimation of tissue densities and electron densities through DE decomposition techniques, overcoming uncertainties in single-energy CBCT's Hounsfield Unit (HU) to density conversions[39,45–49]. These improvements support adaptive radiation therapy where treatment plans can be adjusted based on daily anatomical variations, enhancing dose delivery accuracy and patient outcomes[36].

Markerless tumor tracking is another significant advancement enabled by DE imaging, addressing limitations of fiducial markers by allowing real-time monitoring of tumor motion[50]. This not only improves treatment accuracy but also enhances patient comfort by eliminating invasive procedures to implant the fiducials. DE-CBCT techniques enable continuous tracking of tumor position and shape changes, crucial for adapting treatment strategies and ensuring optimal target coverage. Studies on DE-fluoroscopy techniques have already been investigated[51–53], and findings could be extended to other imaging modalities. This is incredibly relevant to the overall topic of this thesis, as it pertains to markerless tumor tracking of a moving lung tumor.

1.6.5 Stereoscopic Imaging

Stereoscopic imaging is an imaging technique that employs two x-ray sources to generate three-dimensional images, offering detailed information about the tumor's position and movement. The enhanced spatial accuracy provided by stereoscopic imaging significantly improves the precision of radiation dose delivery compared to CBCT, thereby optimizing treatment efficacy and minimizing damage to surrounding healthy tissues.

Several advanced stereoscopic imaging systems are employed in clinical practice, each with unique features and benefits tailored to specific radiotherapy needs. The CyberKnife system (Accuray)[54,55] utilizes a robotic arm to deliver high-dose radiation with sub-millimeter accuracy from multiple angles around the patient. It integrates stereoscopic imaging to track the tumor in real-time, adapting the treatment plan to account for patient movement, particularly respiratory motion. The system's precision makes it highly effective for treating tumors that move with respiration, such as those in the lungs, liver, and prostate.

The SyncTraX system (Shimadzu)[56] addresses geometric and dosimetric uncertainties caused by tumor motion during respiration by using two x-ray tubes and two color image intensifiers to acquire fluoroscopic images from two directions. The system automatically extracts the position of fiducial markers near the tumor, calculating their three-dimensional coordinates. SyncTraX gates the treatment beam based on the absolute 3D position of these markers, ensuring the megavoltage beam activates only when the tumor is within the predefined gating window. This reduces the need for large internal margins, minimizing radiation exposure to healthy tissues and reducing complication risks. The system's wide dynamic range enhances image clarity, particularly in the heart and spine regions, making it an effective tool for precise respiratory-gated radiotherapy.

ExacTrac (Brainlab) (Fig. 1.21) is a room-mounted (i.e., fixed geometry) stereoscopic imaging system that employs a dual x-ray setup, capturing images from two oblique views that are processed to triangulate the tumor's position accurately. The ExacTrac system also incorporates infrared tracking, which enhances its accuracy by monitoring external markers on the patient's body, correlating these movements with internal tumor motion. ExacTrac's combination of x-ray and infrared tracking systems provides a comprehensive solution for tumor localization and motion management. A notable benefit that stereoscopic systems have over CBCT is how projection x-ray images offer faster acquisition and lower doses (e.g., ExacTrac doses of about 0.52 mGy versus typical CBCT doses around 20 mGy[57,58]).

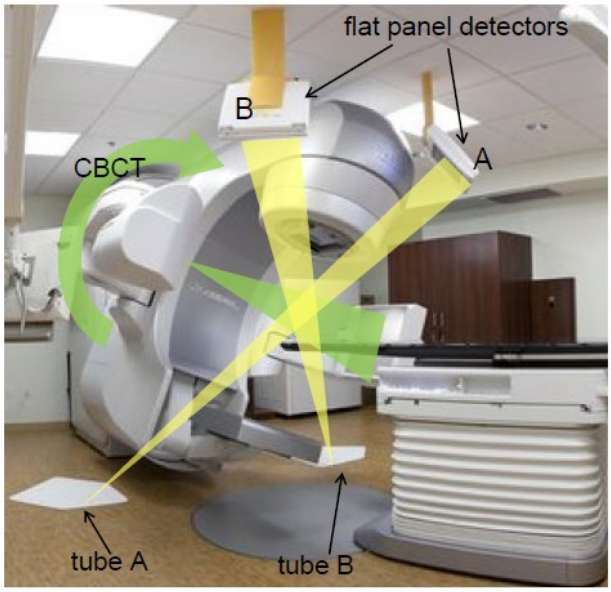

Figure 1.21: The ExacTrac room-mounted stereoscopic imaging system.

The ExacTrac system faces certain challenges, particularly related to maintaining clear imaging during treatment. One significant issue is the potential obstruction of x-ray beams by the rotating gantry of the linear accelerator[59–61]. This obstruction can occur when the gantry moves into positions that block the line of sight between the x-ray tubes and the detectors, compromising image acquisition. To address this, careful planning of gantry angles and x-ray acquisition timing is essential. Additionally, integrating ExacTrac with other imaging modalities, such as cone-beam computed tomography (CBCT), can offer complementary information, ensuring continuous and accurate tumor tracking throughout the treatment session.

Another issue with ExacTrac pertains to how the correlation between infrared-tracked external marker movements and internal tumor position has been shown to be unreliable in some studies[32,33]. Ongoing research and technological advancements aim to improve the robustness of these correlations, ensuring consistent and precise treatment delivery. This includes developments in markerless tracking techniques[24–29], which seek to eliminate the need for external markers and further enhance the accuracy and convenience of the system.

1.7 Thesis Outline

The foundational principles of x-ray imaging systems and their role in modern radiotherapy have been explored in this introductory chapter. The essential components of x-ray tubes, detectors, and the imaging process have been discussed, highlighting their application in guiding precise cancer treatments. The integration of x-ray imaging with advanced radiotherapy techniques has been emphasized, demonstrating the significance of real-time imaging for accurate tumor localization and treatment delivery.

The second chapter will present a comprehensive research manuscript focusing on the development of a novel markerless real-time dual-energy tumor localization technique. This chapter addresses the practical challenges encountered in clinical settings, particularly real-time tumor monitoring and the obstruction caused by rotating gantries in stereoscopic imaging systems. Detailed methodologies, experimental findings, and their clinical implications will be thoroughly discussed, aiming to enhance tumor monitoring during radiotherapy. Included alongside the manuscript are explorations of other 3D localization methods, including epipolar constraints and the Kalman filter.

Finally, the third chapter will summarize the results of the work described throughout this thesis. It will also outline avenues for further research, including the immediate next steps to take based on the results of the manuscript.

Chapter 2: Real-time dual energy markerless monitoring of lung tumors using a clinical room-mounted stereoscopic and monoscopic x-ray imaging system

The content of this chapter is partially based on a manuscript submitted to Medical Physics: "Real-time dual energy markerless monitoring of lung tumors using a clinical room-mounted stereoscopic and monoscopic x-ray imaging system", Zakary McLure, Chris Peacock, Mike Sattarivand. Kalman and epipolar implementations were not part of the manuscript submission.

2.1: Abstract

Background: The motion of lung tumors during breathing poses challenges in stereotactic body radiotherapy (SBRT), warranting improved monitoring techniques. Breathing complicates SBRT by creating positional uncertainty in the lungs, traditionally managed with PTV margins, respiratory gating, or breath hold, each with significant drawbacks. While external and implanted markers for tracking have limitations, dual energy (DE) imaging offers a non-invasive, markerless solution that enhances soft tissue contrast and improves real-time tumor localization accuracy and precision.

Purpose: This study aims to develop a markerless real-time dual energy tumor localization technique on a clinical room-mounted x-ray image guidance system to allow precise 3D stereoscopic and monoscopic lung tumor motion monitoring during radiotherapy.

Methods: A motorized programmable breathing phantom combined with an anthropomorphic phantom was developed to simulate a lung tumor's respiratory motion, with various tumor models (6.4 - 25.4 mm). Real-time images were acquired with a clinical ExacTrac stereoscopic imaging system at a rate of 1.67 Hz with high and low energies (140 & 60 kVp). Weighted logarithmic subtraction and an anti-correlated noise reduction algorithm were used to generate dual energy images. Conventional single energy images (120 kVp) were acquired for comparison. Digital reconstructed radiographs from x-ray imaging views were created to serve as templates for a template-matching algorithm developed to localize tumor locations on x-ray views. For the stereoscopic case where both imaging views were available, 3D triangulation was performed to localize the tumor. In the monoscopic case, when only one x-ray view was

available, the 3D tumor position was estimated using a single 2D localization, combined with a 3D probability density function (PDF) describing tumor motion.

Results: Stereoscopic dual energy techniques demonstrated accurate localizations. The monoscopic view obstructed by the spinal cord showed lower success rates than the view obstructed only by the rib bone. In the stereoscopic cases, dual energy consistently outperformed single energy methods, successfully localizing a minimum of 92% of positions for all tumor sizes, compared to 50% for single energy. Both dual and single energy PDF estimates for the monoscopic region obscured by the ribs showed a 100% success rate for all tumor sizes, except the smallest tumor for single energy, having only 57% localization success. The other monoscopic region, obscured by the spine, showed 100% localization success for only the largest tumor size, but consistently showed improvements of up to 20% for the dual energy over single energy technique (93% vs 73% for the 12.7 mm tumor).

Conclusions: A real-time markerless tumor monitoring technique was developed utilizing a clinical room-mounted stereoscopic / monoscopic image guidance system. Dual energy increases the accuracy of successful tumor localization as compared to the conventional single energy approach, especially for smaller tumors. The use of PDFs may be a viable approach to monoscopic estimates when only one view is available.

2.2: Introduction

Lung tumors exhibit motions of up to 3 cm during a regular breathing cycle[18–20]. This is especially undesirable for cancer patients undergoing stereotactic body radiotherapy (SBRT), where large doses are delivered in a small number of fractions[62]. Breathing motion creates positional uncertainty, which is traditionally managed by increasing planning target volume (PTV) margins[21], respiratory gating[22], or breath hold[23]. The former increases unwanted dose delivery to nearby healthy organs at risk (OARs) as it requires large margins to define an internal target volume (ITV)[63]. The latter two increase treatment time, require patient compliance, and can cause strain and discomfort to patients, especially those with respiratory conditions[22,23,64]. Preferred approaches would involve direct real-time monitoring of tumor motion.

Monitoring tumor motion can be performed through tracking body surface markers as a

surrogate to internal target motion[30]. However, the correlation between external markers and lung tumor motion has been shown to be unreliable due to intra-fractional drift[31]. A more direct technique uses implanted radio-opaque markers on the target volume[65]. Implanting these markers is invasive and can cause pneumonitis or pneumothorax[32,33]. Additionally, studies have shown that the fiducial markers may drift more than 2.5 mm between fractions, affecting localization accuracy[32,33]. Consequently, there is a growing demand for real-time non-invasive, markerless lung tumor monitoring.

Markerless tumor monitoring techniques have been explored[24–27], notably those using template matching algorithms during treatment[28,29]. However, bony anatomy in the imaging field can hinder such localization tactics, which themselves rely on the high contrast between the tumor and surrounding tissue. The problem of tumor obstruction by bone can be addressed using dual energy (DE) imaging instead of conventional single energy (SE) techniques to suppress bone contrast and enhance soft-tissue-only images, thereby improving localization accuracy and precision[52,54,68–70].

Room-mounted stereoscopic imaging systems such as ExacTrac (Brainlab AG, Germany) can be utilized to provide real-time, sub-millimeter accurate views of the treatment volume to monitor prostate motion using implanted fiducials[66], but they currently provide no reliable method for intra-fraction lung tumor monitoring. Additionally, in a typical lung SBRT treatment, one of the two x-ray imagers of the stereoscopic imaging system will be blocked by the rotating linac gantry during volumetric arc therapy (VMAT) treatment, hindering exact 3D location from a single 2D perspective. Recent developments in monoscopic (single view) localization of fiducial markers in prostate tumors for gantry mounted kV imaging systems offer a solution by correlating between motions in the anterior-posterior and inferior-superior directions to generate an informed estimate of the third dimension[59–61]. This approach may also be extended to the context of lung tumors.

To our knowledge, there has not yet been a study that combines bone-suppression from dual energy imaging with stereoscopic and monoscopic 3D localization for continuous lung tumor monitoring during treatment. The objective of this study is to develop a real-time markerless tumor monitoring technique for stereoscopic imaging systems to monitor lung tumor motion during treatment, while also addressing the issue of intermittent monoscopic scenarios created by the rotating gantry.

2.3: Materials and Methods

2.3.1: Data Acquisition

2.3.1A: Phantom Design and Experiment Setup

To emulate lung patient anatomy, an anthropomorphic breathing phantom (TBP, Mirion Technologies NJ, USA) was used. Soft tissue thickness was increased by positioning a 5 cm thick plate of Lexan polycarbonate resin beneath the phantom. The built-in expanding lung insert was removed, and an attached tumor model was inserted into the phantom's chest cavity (Figure 2.1a). Tumors were modeled using four spherical acrylic targets (Plastic World, ON, Canada) with diameters of 6.4 mm, 12.7 mm, 19.1 mm, and 25.4 mm. Realistic lung tumor motion was achieved by repurposing a motor from a Quasar respiratory motion phantom (Modus medical devices, London, ON, Canada) and feeding to it a realistic typical lung motion (see section 2.3.1B). The Quasar phantom was mounted on a platform supporting the Lexan plate and breathing phantom at a fixed position on the treatment couch. Computed tomography (CT) images of each tumor (while at rest within the phantom) were acquired with a clinical CT simulator using institution's lung SBRT imaging protocol (2.50 mm slice thickness).

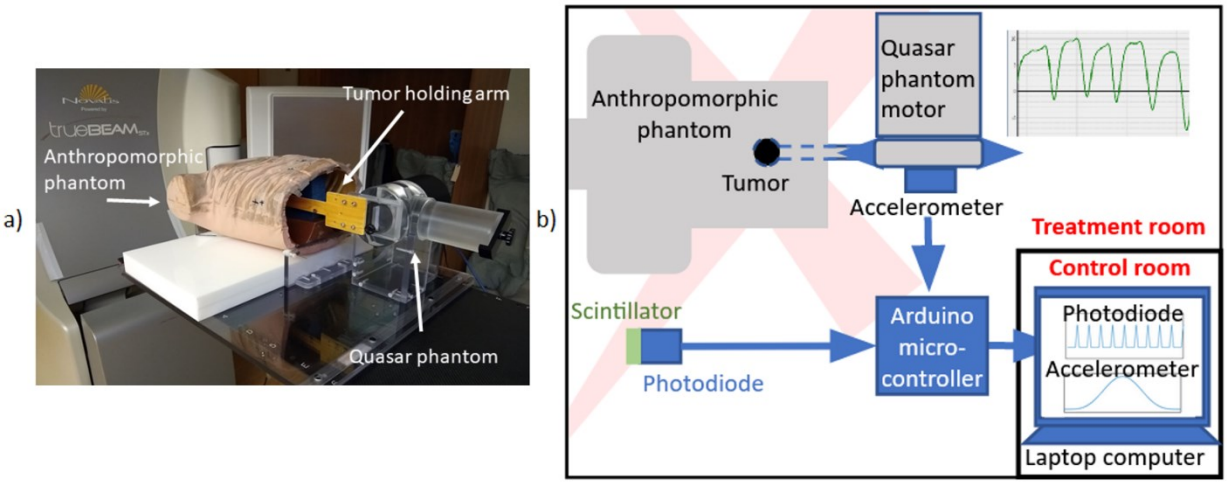

Figure 2.1: a) The experimental phantom setup used for the real-time motion experiment. b) A schematic depicting the electronics used for the real-time motion experiment. The shaded pink regions represent the stereoscopic x-ray beams. A section of the applied realistic breathing motion pattern is plotted at the top-right corner.

2.3.1B: Real-time Imaging Data Acquisition

For each tumor size, the attached spherical tumor model was aligned with the treatment room isocenter using the room lasers. Employing the Quasar motor motion program, the tumor followed a predefined trajectory based on input data containing typical lung breathing motion patterns. This data was sourced from the markerless lung target tracking AAPM Grand Challenge (MATCH)[67] and used as a ground truth. Due to current hardware constraints of the existing ExacTrac system, rapid switching of tube voltages between successive image captures was not performed. Instead, two sets of real-time images were acquired for high and low energy sequences during two separate (but identical) breathing cycles and were subsequently used to generate dual energy images. To synchronize tumor motion with image acquisition, a photodiode (TCS34725, Adafruit Industries, New York USA) coupled with 5 mm thick scintillating material (EJ-208, Eljen Technology, Texas USA) was positioned on the floor to detect x-ray beam pulse (Figure 2.1b). A MATLAB script (MathWorks, Natick, MA) initiated tumor motion from a fixed start position upon detecting the first x-ray pulse. An accelerometer (SEN-12786, SparkFun Electronics, Colorado USA) attached to the tumor motion arm, outside of the field of view, measured the delay between x-ray pulse and tumor motion initiation. Both the accelerometer and photodiode communicated with an Arduino microcontroller (SparkFun, CO, USA) via I2C connector cables. The microcontroller combined the readings and transmitted them as a single byte of data via a USB cable to a laptop, where they were saved to a text file. The detected motion delay was determined to be 110±7 ms, therefore the motor response time was considered negligible.

For each of the four tumor sizes, real-time stereoscopic DE and SE imaging series were acquired at an imaging frequency of 1.67 Hz using a clinical ExacTrac (Brainlab) imaging system (Ver 6.2). Each series took 60 seconds to acquire and consisted of 100 imaging frames. The imaging parameters for the DE images were (140 kVp, 8 mAs) for high energy and (60 kVp, 25 mAs) for low energy acquisitions. These acquisition techniques were optimal dual energy parameters based on a previous study for lung patients to maximize tumor contrast in DE images, while ensuring that the total dose from dual energy does not exceed that of single energy[57]. The real-time SE images were acquired using (120 kVp, 16 mAs) imaging parameters. This acquisition technique was chosen based on vendor recommendations for lung patient imaging[68].

2.3.2: Data Analysis

2.3.2.1: Dual Energy Image Generation

For each frame in the real-time image series, a soft-tissue-only dual energy image I_{DE}^{ST} was calculated using a weighted log subtraction of the corresponding low energy image I_{LE} from the high energy image I_{HE} (equation 2.1). Similarly, bone-only DE images I_{DE}^{B} were generated for use in an anti-correlated noise reduction algorithm (ACNR)[15] (equation 2.2) which was applied to reduce noise in the soft-tissue dual energy images.

$$\log(I_{DE}^{ST}) = \log(I_{HE}) - \omega \log(I_{LE}) \qquad (2.1)$$
$$\log(I_{DE}^{B}) = -\log(I_{HE}) + \omega_b \log(I_{LE})$$

$$\log\left(I_{DE,ACNR}\right) = \log(I_{DE}^{ST}) + \omega_n \log(I_{DE}^{B}) * h_{HPF} \qquad (2.2)$$

Here, h_{HPF} is a Gaussian high pass filter with a lower cutoff frequency of[14] 0.2 pixel^{-1}. The noise suppression weighting factor ω_n was set to 0.9 for the calculation of all DE images[14]. The soft tissue DE weighting factor ω was chosen for each imaging frame and for both stereoscopic views by varying ω until bone suppression was maximized around the tumor. For tube A, this was done quantitatively by selecting an ROI that encompassed both a rib and its surrounding soft tissue, then varying ω until the CNR within the ROI was minimized. Similarly, the bone-only DE weighting factor ω_b was chosen by varying ω_b to achieve the highest soft tissue suppression around the tumor while maximizing bone contrast for each frame. An ROI was chosen to encompass the tumor and an adjacent rib, then ω_b was varied until the bone only image had a minimized CNR within the ROI. No ROIs were used for the tube B point of view, and a qualitative evaluation of the ω values was performed instead. The ω range was [0.7-0.8] and [1.08-1.12] for the two stereoscopic images from tubes A and B respectively. Larger weighting factors were required for image from tube B than tube A due to presence of thicker bone (spine) in view B compared to rib in view A. Similarly, the range for the bone-only weighting factor ω_b was [1.35-1.40] and [1.65-1.70] for tubes A and B respectively.

2.3.2.2: Template Matching

Figure 2.2 describes the template matching procedure. The CT images of the tumors and phantom were exported to a commercial contouring and treatment planning system (Eclipse, Varian Medical Systems, Inc., Palo Alto, USA). Here, the gross tumor volume (GTV) was manually contoured for each of the four tumor sizes. Both the CT images and resulting contours were then exported in DICOM format from Eclipse to an in-house MATLAB code, where tumor-only CT images were generated by masking out the non-tumor volume. Using a custom MATLAB script, tumor templates for each tumor size were created by generating digitally reconstructed radiographs (DRRs) from each tumor-only CT image, simulating the beam's eye views of the ExacTrac stereoscopic imaging system[69,70]. The tumor templates were then cropped from the DRRs, with the cropping region centered on the tumor's center of mass.

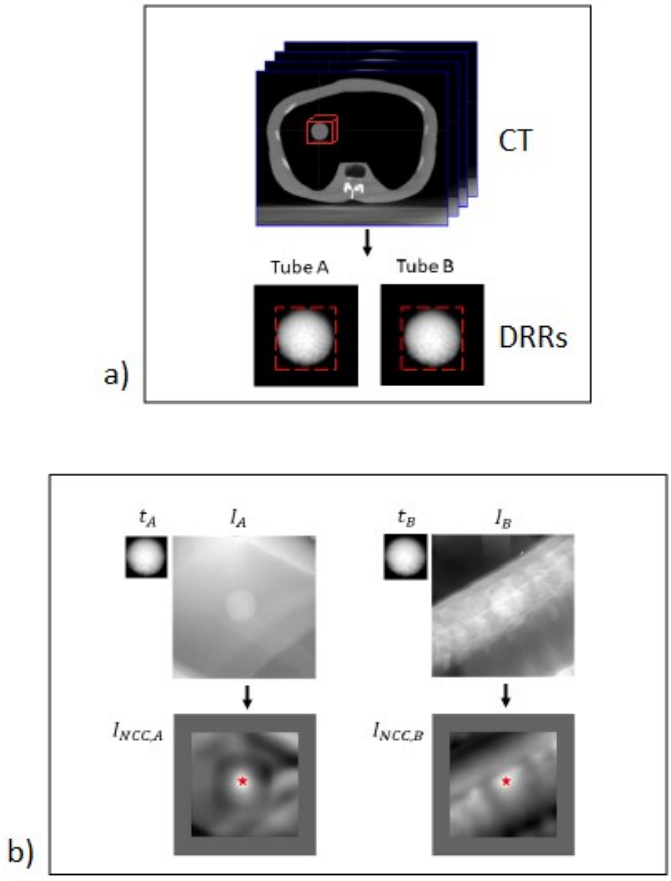

Figure 2.2: Description of the template matching procedure. (a) Template generation: Crop region around the tumor from CT and calculate DRR of the tumor for each stereoscopic imaging view. (b) Normalized cross-correlation template matching using the DRR templates and the acquired SE or DE images. Return the global maxima of both correlation images as the optimal match positions.

As per Mostafavi et al.[28], normalized cross correlation was used as a metric for template matching localization for each stereoscopic view. This algorithm was implemented using the MATLAB function *normxcorr2*, which calculates the normalized cross-correlation between a template image t and a search image I using equation 2.3:

$$I_{NCC}(u,v) = \sum_{x,y} \frac{(I(x,y)-\bar{I}_{u,v})(t(x,y)-\bar{t})}{N\sigma_I\sigma_t}, \quad (2.3)$$

where $\bar{t}$ represents the average pixel value of the template, while $\bar{I}_{u,v}$ indicates the average pixel value within the template-sized region of the image I, centered at pixel position (u,v). N denotes the total number of pixels in the template t. σ_t and σ_I represent the pixel standard deviation for the template and the sub-image centered at position (x,y) respectively. To maintain the original image size within the cross-correlation image I_{NCC}, I was padded with $N_x/2$ columns and $N_y/2$ rows of zeros. The global maximum position of I_{NCC} for each stereoscopic projection image was selected to determine the tumor's location within each imaging view.

2.3.2.3: Three-Dimensional Tumor Localization

A typical lung SBRT treatment using volumetric arc therapy (VMAT) requires ipsilateral treatment arcs. This is illustrated in Figure 2.3 for a right lung case where gantry angle may range from -180° to 10°. The gantry motion during the treatment arc will cause real-time ExacTrac imaging to go through periods of stereoscopic (where both views are available) or monoscopic (only one view available) imaging. Figure 2.4 describes the workflow for image acquisition and 3D tumor localization depending on whether the gantry blocks one of the stereoscopic imaging views. In all scenarios, the template matching algorithm (described in section 2.3.2.2) was used to locate the tumor in each 2D x-ray image view. Stereoscopic triangulation, described in section 2.3.2.3.1, was used in the cases where both imaging views were available. Monoscopic localization with a probability density function (PDF) approach, described in section 2.3.2.3.3, was used when only one imaging view was available.

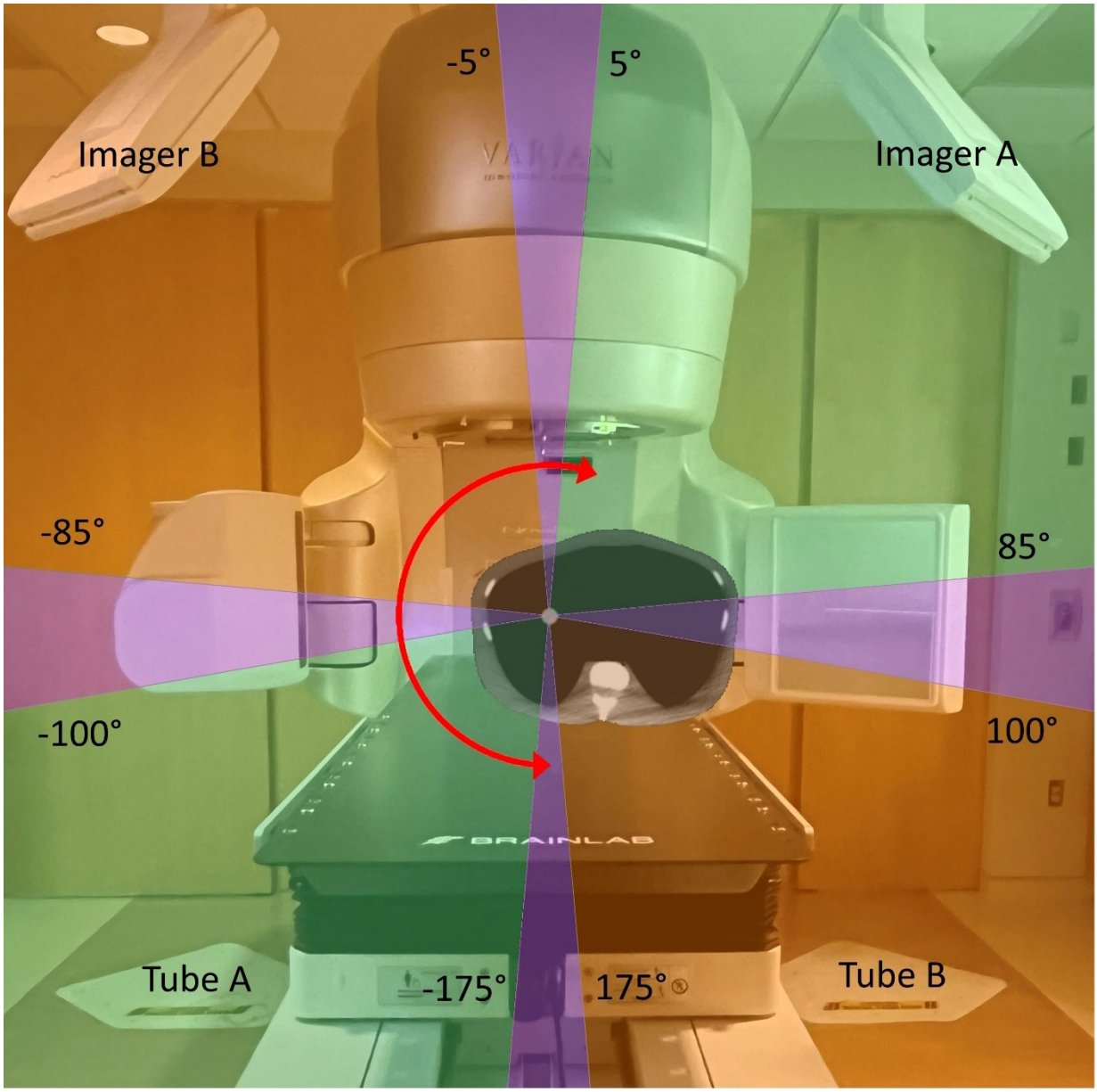

Figure 2.3: Monoscopic (green/orange) and stereoscopic (purple) regions defined by the gantry angle during the treatment arc (red) of a lung SBRT patient. In the green regions, the gantry obstructs view A and in the orange regions, view B is blocked, thus monoscopic imaging is possible with either view in these regions.

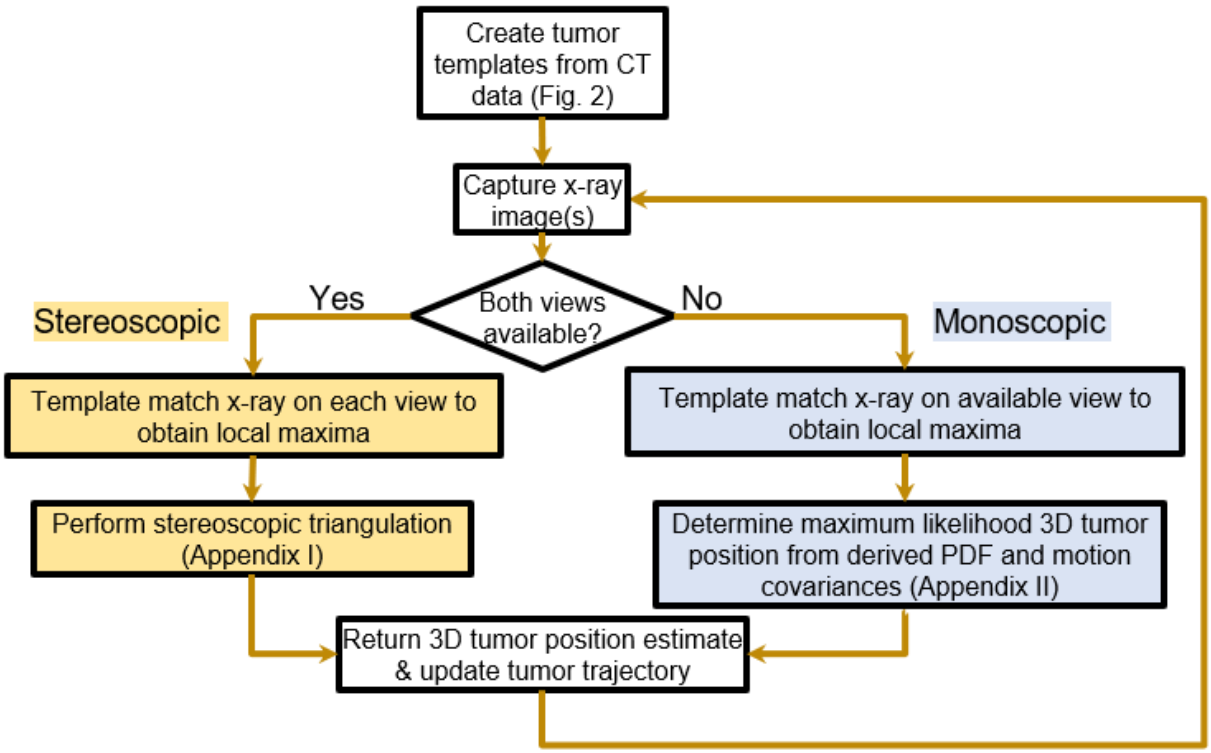

Figure 2.4: Flowchart describing image acquisition for 3D localization estimates. The stereoscopic and monoscopic approaches are described in section 2.3.2.3.1 and 2.3.2.3.3 respectively.

Three-dimensional localization positions were compared to the ground truth to calculate accuracy and precision. For each frame, a 3D localization was considered successful if the tumor was found within 5 mm of the ground truth[51]. The localization accuracy and precision along the anterior-posterior, left-right, and superior-inferior directions were calculated using the mean and the standard deviation of the difference between the successfully localized tumor position and the ground truth respectively.

2.3.2.3.1: Stereoscopic localization using 3D triangulation

Adopting a stereoscopic triangulation methodology akin to Wei et al.[71], the 3D localization of the tumor was determined by identifying the shortest line segment connecting two back-traced rays, which originate from a pair of 2D tumor localizations (determined using template matching as per section 2.3.2.2). Referring to Figure 2.5a with known orientation (polar angle θ and azimuthal angle Φ) and inter-pixel spacing for each imaging panel i, the relationship

between the 2D position of a pixel on the panel (x_{im}, y_{im}) and the corresponding point on room 3D coordinates $\vec{p}_i$ is expressed by the following equation:

$$\vec{p}_i = R \cdot \begin{bmatrix} x_{im}^i \\ y_{im}^i \\ 0 \end{bmatrix} \cdot \frac{SDD}{SAD} \tag{2.4}$$

where SDD (source to detector distance) and SAD (source to axis/isocenter distance) are used as a scaling factor, and $R = R_x \cdot R_y$ is a matrix used to rotate the detector coordinate system to the room coordinate system. The rotation matrices R_x and R_y are defined in equation 2.5.

$$R_x = \begin{bmatrix} 1 & 0 & 0 \\ 0 & \cos(90° - \theta) & -\sin(90° - \theta) \\ 0 & \sin(90° - \theta) & \cos(90° - \theta) \end{bmatrix}, R_y = \begin{bmatrix} \cos(\Phi) & 0 & \sin(\Phi) \\ 0 & 1 & 0 \\ -\sin(\Phi) & 0 & \cos(\Phi) \end{bmatrix} \tag{2.5}$$

For ExacTrac imaging panels A and B, $\theta_A = \theta_B = 48°$, $\Phi_A = -45°$, and $\Phi_B = 45°$. Likewise, the SDD and SAD are 343.5 cm and 218.5 cm respectively[70]. Given a pair of 2D image coordinates $[x_{im}^A, y_{im}^A]$ and $[x_{im}^B, y_{im}^B]$ obtained from template matching applied to each of the x-ray images, points $\vec{p}_A$ and $\vec{p}_B$ can be derived. The triangulation process proceeds by using the pair of vectors between the x-ray sources and their respective panel detectors to determine the most probable 3D position where the pair of back-traced rays would intersect (Figure 2.5b). $\vec{P}_A$ and $\vec{P}_B$ represent the points on the source-detector ray, defining the shortest crossline distance between the two rays. These points are determined by scaling the unit vector for each source-detector pair $\hat{r}_A$ and $\hat{r}_B$ by scalars L_A and L_B, originating from the pixel positions $\vec{p}_A$ and $\vec{p}_B$ respectively:

$$\begin{aligned} \vec{P}_A &= L_A \hat{r}_A + \vec{p}_A \\ \vec{P}_B &= L_B \hat{r}_B + \vec{p}_B \end{aligned} \tag{2.6}$$

where $\hat{r}_A = \frac{\vec{I}_A - \vec{p}_A}{|\vec{I}_A - \vec{p}_A|}$, $\hat{r}_B = \frac{\vec{I}_B - \vec{p}_B}{|\vec{I}_B - \vec{p}_B|}$, and $\vec{I}_A$ and $\vec{I}_B$ are source points on Tube A and B respectively. The proposed method suggests the most probable 3D ray coincidence point to be the midpoint along the shortest line segment between the two rays. This midpoint is determined by locating

the halfway point along a line connecting the two rays and perpendicular to both. The shortest line segment $\vec{d}$, connecting points $\vec{P}_A$ and $\vec{P}_B$, is computed by projecting the vector connecting points $\vec{p}_A$ and $\vec{p}_B$ onto a unit vector that is perpendicular to both $\hat{r}_A$ and $\hat{r}_B$:

$$\vec{d} = \left((\vec{p}_A - \vec{p}_B) \cdot \frac{\hat{r}_A \times \hat{r}_B}{|\hat{r}_A \times \hat{r}_B|} \right) \frac{\hat{r}_A \times \hat{r}_B}{|\hat{r}_A \times \hat{r}_B|} \tag{2.7}$$

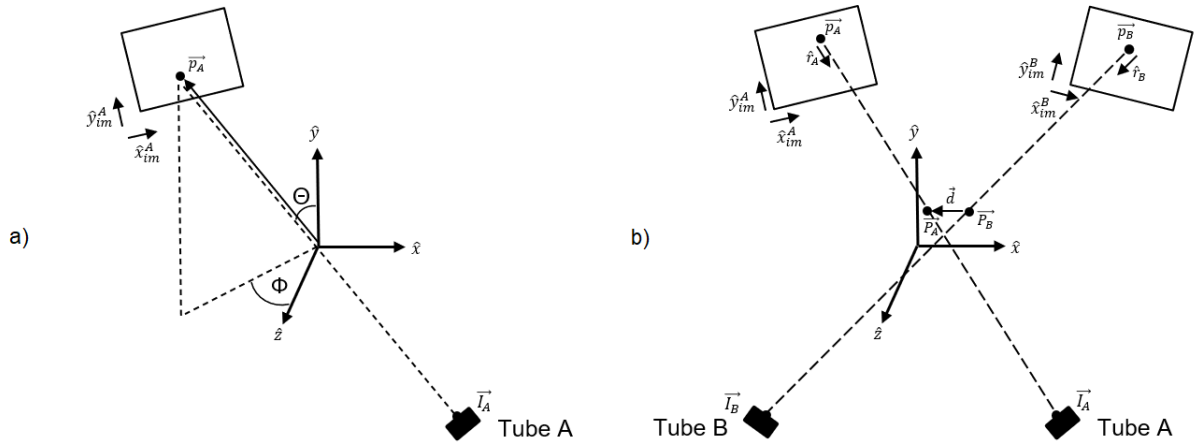

Figure 2.5: a) ExacTrac detector geometry polar angle θ and inclination Φ, with respect to treatment room coordinates, using the ray-traced line between view A and Tube A. b) Illustration of how triangulation is performed by determining the shortest crossing line between a pair of vectors traced back from image coordinates to x-ray tubes.

The scaling coefficients L_A and L_B for each of the back-trace unit vectors are derived using equations 2.6 and 2.7 as follows, with the knowledge that $\vec{P}_A = \vec{P}_B + \vec{d}$:

$$L_A\hat{r}_A + \vec{p}_A = L_B\hat{r}_B + \vec{p}_B + \vec{d}$$

$$L_A\hat{r}_A - L_B\hat{r}_B = \vec{p}_B - \vec{p}_A + \vec{d}$$

$$L_A(\hat{r}_A \times \hat{r}_B) - L_B(\hat{r}_B \times \hat{r}_B) = \left(\vec{p}_B - \vec{p}_A + \vec{d}\right) \times \hat{r}_B$$

$$L_A = \frac{\left|\left(\vec{p}_B - \vec{p}_A + \vec{d}\right) \times \hat{r}_B\right|}{|\hat{r}_A \times \hat{r}_B|}$$

A similar approach is used to isolate L_B. The scaling coefficients are therefore:

$$L_A = \frac{\left|\vec{D} \times \hat{r}_B\right|}{|\hat{r}_A \times \hat{r}_B|} \qquad (2.8)$$

$$L_B = \frac{\left|\vec{D} \times \hat{r}_A\right|}{|\hat{r}_B \times \hat{r}_A|}$$

where $\vec{D} = \vec{p}_B - \vec{p}_A + \vec{d}$. The center point between A and B is calculated as the average of the two points $\vec{v} = \frac{\vec{P}_A + \vec{P}_B}{2}$.

2.3.2.3.2: Epipolar Geometry

During the stereoscopic case, when both views are available, it may prove beneficial to assign different weightings that describe how much one view influences the triangulation algorithm versus the other. Factors such as presence of significant anatomical noise (more bone overlap) could contribute to the determining of such weighting factors. Epipolar geometric constraints may be a potential solution to such concerns.

In stereoscopic imaging, where system geometry is known, the position of an object in one imaging view corresponds to a unique epipolar line of possible object locations in the complementary view (see Fig. 2.6). The epipolar line constraint has been used to improve 3D triangulation in computed tomography[72] and to track patient motion using multi-view imaging systems[73]. It has also been applied to aid lung tumor tracking and pre-treatment image alignment in clinical systems like the Xsight[74] and Vero[75]. The benefit of using an epipolar constraint for tracking tumors of various sizes has not yet been examined, but it is expected to reduce incorrect localizations due to limiting regions within which template matched pixel coordinates may exist. By assigning a higher weight to a stereoscopic view with lower anatomical noise, the epipolar constraint should in theory filter out problematic points on complementary views with more bone obstructions (e.g., rib vs. spine).

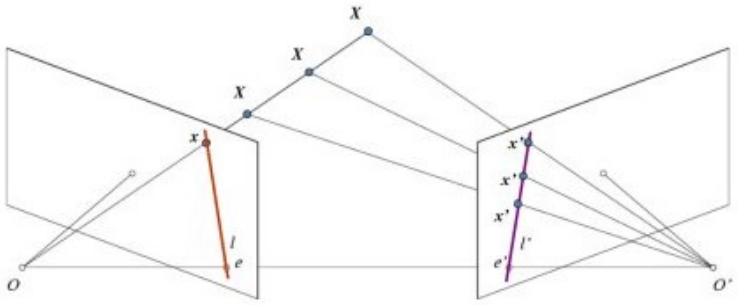

Figure 2.6: Demonstrating the epipolar constraint for two stereoscopic views. An object viewed at x in the left view must have a corresponding position x' on the right view.[76]

An algorithm[77] outlined in Figure 2.7 incorporating an epipolar constraint was developed as an extension to the template matching and stereoscopic triangulation algorithms highlighted earlier in sections 2.3.2.2 and 2.3.2.3. This algorithm was applied to both SE and DE x-ray images. First, a pair of stereoscopic images corresponding to each x-ray tube (I_A and I_B) are processed with a local median filter to reduce pixel noise. This reduction of noise assists template matching by removing outlier pixels and improving CNR. Next, a normalized cross-correlation is computed for each filtered image ($I_{A,med}$ and $I_{B,med}$) with their corresponding templates, producing correlation score images C_A and C_B. Local maxima lower than $C_{thresh} = 0.7 * \max(C_A, C_B)$ [77] in these correlation images are identified and filtered by a threshold to generate lists of candidate points p_A and p_B.

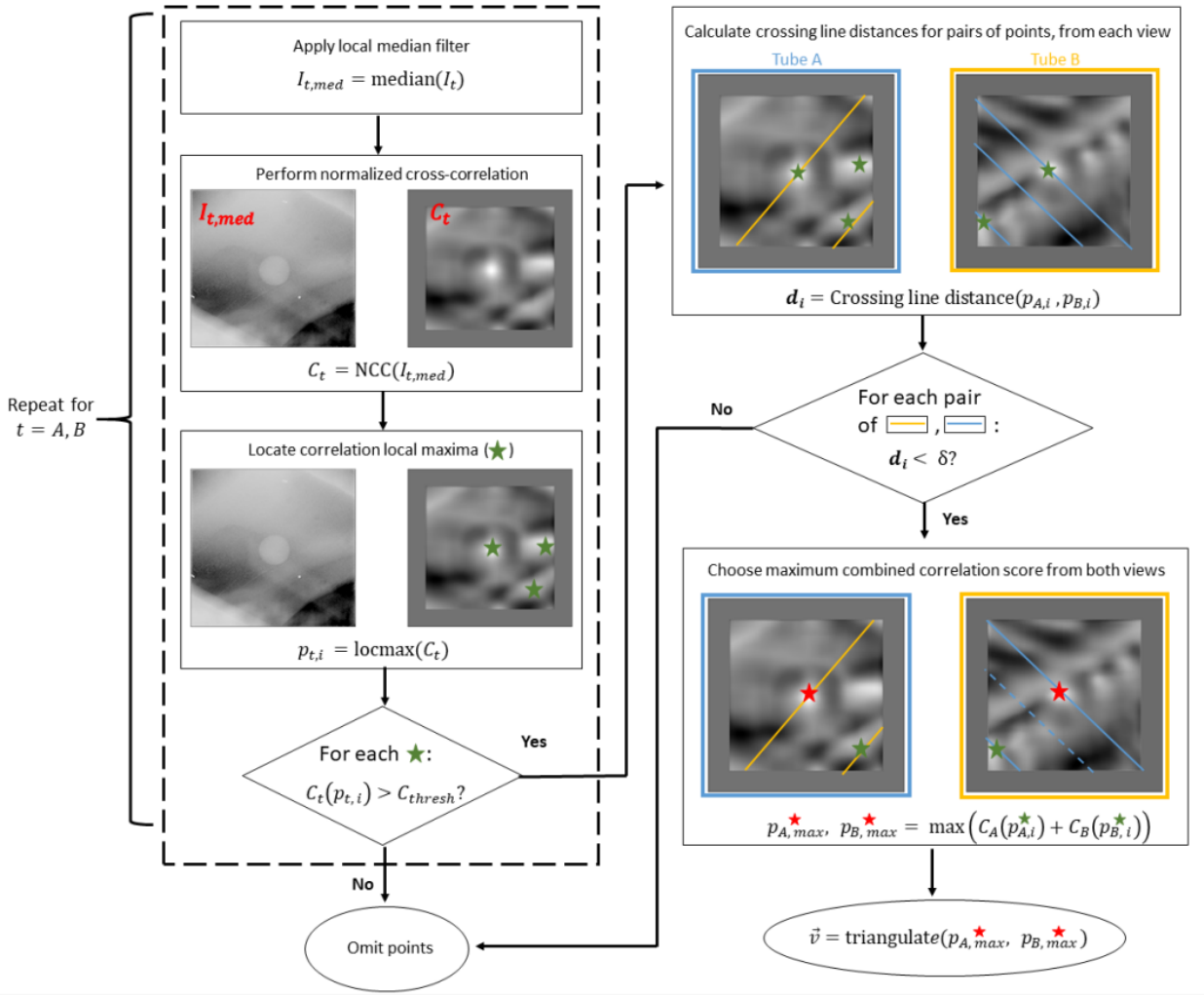

Figure 2.7: Epipolar constraint algorithm flowchart. The lines crossing the images indicate the required series of positions according to localizations from the opposite image. These are known as epilines.[77]

Each pair of points from these lists is back traced to the respective x-ray source, and the shortest crossing line distances are computed, forming a matrix of crossing line distances. Pairs with distances below a crossing line distance threshold ($\delta = 2$ mm)[77] are considered as potential 3D tumor locations. The sum of correlation scores for these pairs is calculated, and the pair with the highest combined score is selected as the best 2D template match positions. The optimal 3D tumor position is then determined by triangulating these points as described in section 2.3.2.3.1. If no pairs pass the crossing line distance threshold, the correlation threshold is reduced by 10%, and the process is repeated.

2.3.2.3.3: Monoscopic Localization

The use of a Gaussian probability density function (PDF) to estimate a 3D position in monoscopic imaging using on-board imagers is described by Poulsen et al.[59] and was replicated by Stevens et al. for the ExacTrac system in the context of prostate tumors[66]. The method depicted in Figure 2.8 requires *a priori* information in the form of motion covariances Q. These covariances can either be derived from the patient-specific real-time tumor localization before treatment, or from established patient population averages. The latter is expected to be less accurate as it represents the population average. Therefore, in this study, patient-specific covariances were calculated using the tumor motion estimated by stereoscopic localization from all 100 frames as per section 2.3.2.3.1.

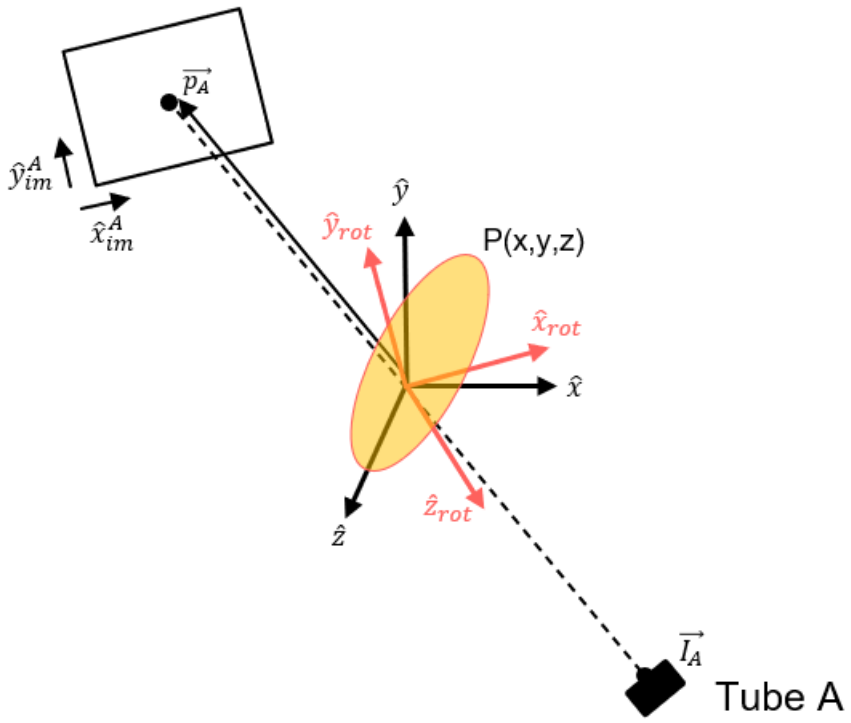

Figure 2.8: Monoscopic localization uses a Gaussian PDF derived from motion covariances to determine the maximum likelihood position (orange ellipsoid) along the ray-traced line between the x-ray source $\overrightarrow{I_A}$ and the 2D imager point $\overrightarrow{p_A}$ obtained from template matching. Lung motion is most prevalent in the SI (z) direction.

$$Q = \begin{bmatrix} var_x & cov_{xy} & cov_{xz} \\ cov_{xy} & var_y & cov_{yz} \\ cov_{xz} & cov_{yz} & var_z \end{bmatrix} = \begin{bmatrix} 0.0695 & 0.0281 & 0.1929 \\ 0.0281 & 0.0273 & 0.1734 \\ 0.1929 & 0.1734 & 19.3994 \end{bmatrix} mm^2 \quad (2.9)$$

By using this covariance matrix, the PDF for the tumor positions $P(x, y, z)$ can be determined in a coordinate system rotated to align with the imaging plane, but with the same origin as the patient coordinate[78]. The inverse of the rotation matrix from section 2.3.2.3.1, $R = R_x \cdot R_y$, is applied to the rotated 3D position vector $\vec{r}_{rot} = [x_{rot}, y_{rot}, z_{rot}]$ to determine the 3D room position $\vec{p}_i$,

$$\vec{p}_i = R^{-1} \cdot \vec{r}_{rot} \quad (2.10)$$

where i=A for tube A and i=B for tube B. The Gaussian PDF in the rotated coordinate system aligned with the imaging plane is described by:

$$P_{rot}(x_{rot}, y_{rot}, z_{rot}) = \sqrt{\frac{det(Q^{-1})}{8\pi^3}}\, e^{-\vec{r}_{rot}^T R Q^{-1} R^{-1} \vec{r}_{rot}/2}. \quad (2.11)$$

Representing the elements of the rotated covariance matrix as

$$R^{-1}Q^{-1}R = \begin{bmatrix} A_{rot} & D_{rot}/2 & E_{rot}/2 \\ D_{rot}/2 & B_{rot} & F_{rot}/2 \\ E_{rot}/2 & F_{rot}/2 & C_{rot} \end{bmatrix}, \quad (2.12)$$

the expected value of the position along the axis normal to the imaging plane $\langle z_{rot} \rangle$ is[59]

$$\langle z_{rot} \rangle = SAD \left[A_{rot} \left(\frac{x_{im}}{SDD}\right)^2 + B_{rot} \left(\frac{y_{im}}{SDD}\right)^2 + D_{rot} \frac{x_{im} y_{im}}{SDD^2} - E_{rot} \frac{x_{im}}{2 \cdot SDD} - F_{rot} \frac{y_{im}}{2 \cdot SDD} \right] \sigma^2, \quad (2.13)$$

where SDD represents the source-to-detector distance and SAD is the source-to-isocenter distance, both of which are described in section 2.3.2.3.1. Sigma represents the standard deviation, found using:

$$\sigma = \left[A_{rot}\left(\frac{x_{im}}{SDD}\right)^2 + B_{rot}\left(\frac{y_{im}}{SDD}\right)^2 + C_{rot} + D_{rot}\frac{x_{im}y_{im}}{SDD^2} - E_{rot}\frac{x_{im}}{SDD} - F_{rot}\frac{y_{im}}{SDD}\right]^{-\frac{1}{2}}. \quad (2.14)$$

Adjusting the image coordinates $[x_{im}, y_{im}]$ based on this expectation value allows for the determination of the (rotated) 3D position of the lung tumor $\vec{r}_{rot} = [x_{rot}, y_{rot}, z_{rot}]$

$$x_{rot} = x_{im}\frac{SAD - z_{rot}}{SDD} \quad (2.15)$$

$$y_{rot} = y_{im}\frac{SAD - z_{rot}}{SDD} \quad (2.16)$$

Finally, we use the inverse rotation matrix, shown with equation 2.10, to calculate the 3D monoscopic coordinates.

2.3.2.3.4: Kalman Filter

As will be discussed later in section 2.5, a study by Montanaro et al. examined four types of 2D-3D inference methods when converting a measurement from an on-board kV imaging system to a predicted 3D position, to evaluate real-time target tracking accuracies[79]. They concluded that longer temporal windows (120 – 140 s) would benefit most from PDF-based methods, such as the Gaussian PDF approach used throughout the manuscript in Chapter 2. Short windows on the order of one minute or less would benefit most from the Kalman filter, which combines measurements with a model based on prior knowledge to estimate how a system evolves over time[80] (Fig. 2.9). This section will expand on the Kalman filter and investigate how it may be potentially implemented to improve localization estimates with DE imaging in a stereoscopic setting.

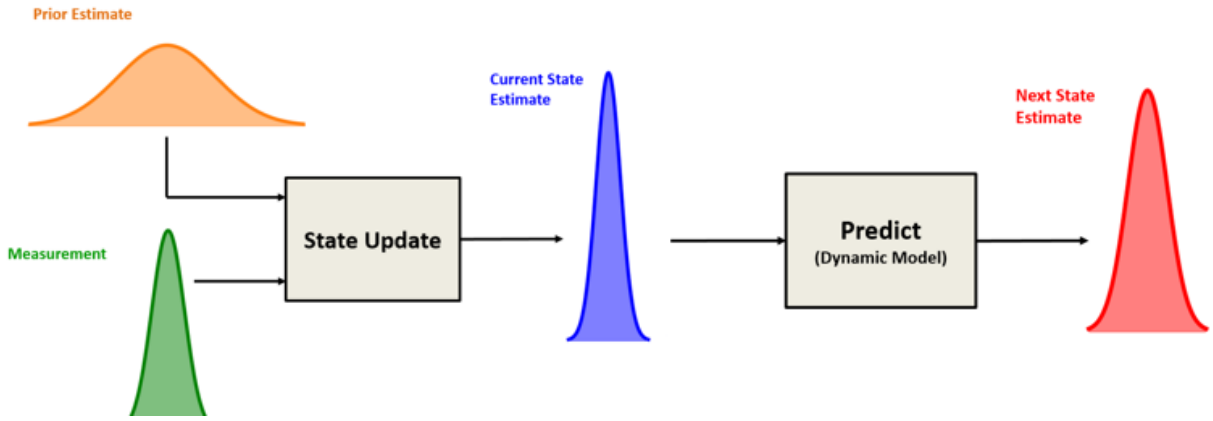

Figure 2.9: Simple visualization of the main components of the Kalman filter. A state estimate is updated via measurement and dynamic model to predict a new state estimate.[81]

The Kalman filter is a recursive algorithm designed to estimate the state of a linear dynamic system from a series of noisy measurements[80]. It operates optimally under the assumptions that the system dynamics and the measurement process are both linear. In other words, the state transition and measurement equations are linear functions of the state and control variables. Additionally, the Kalman filter assumes that both the process noise and measurement noise are Gaussian, that is, characterized by a normal distribution with a specific mean and variance.

2.3.2.3.4A: System Model

Consider a discrete-time linear dynamic system characterized by the state transition and measurement equations. The *state transition equation* is given by[80]:

$$x_k = F_{k-1}x_{k-1} + B_{k-1}u_{k-1} + w_{k-1} \tag{2.17}$$

Here, x_k represents the state vector at time step k. The state vector x_k contains all the information needed to describe the system at time k. For example, in a system that tracks the motion of an object, the state vector might include position, velocity, and acceleration. The matrix F_{k-1} is the state transition matrix, which relates the state at $k-1$ to the state at k. It models how the state evolves over time in the absence of noise and control inputs. For instance, in a simple motion model, F_{k-1} could describe how the position and velocity change from one time step to the next.

The vector u_{k-1} is the control input vector, which represents any external inputs to the system that affect its state. For example, in a vehicle navigation system, u_{k-1} might represent steering commands or throttle inputs. The control input vector introduces the influence of external control actions on the state of the system. The matrix B_{k-1} is the control input matrix, which models how the control inputs affect the state. This matrix maps the control inputs u_{k-1} to the state vector x_k. Essentially, B_{k-1} translates the control actions into changes in the state vector.

The term w_{k-1} represents the process noise, which accounts for any random perturbations affecting the system. This noise is assumed to be Gaussian with zero mean and covariance Q_{k-1}. Process noise can represent various uncertainties, such as modeling errors or external disturbances. It reflects the uncertainty in the system dynamics.

The *measurement equation* is defined as[80]:

$$z_k = H_k x_k + v_k \tag{2.18}$$

In this equation, z_k represents the measurement vector at time step k, containing the observations made about the system. For instance, in a system that tracks an object's displacement, z_k might include measurements of distance and velocity. The matrix H_k is the transformation matrix, which relates the state x_k to the measurement z_k. It models how the true state of the system is observed through the measurement process. Specifically, H_k maps the elements of the state vector to the observed measurements, effectively translating the state space into the measurement space.

The term v_k represents the measurement noise, which accounts for any random perturbations affecting the measurements. This noise is also assumed to be Gaussian with zero mean and covariance R_k. Measurement noise can represent sensor inaccuracies or environmental factors affecting the measurements. It reflects the uncertainty in the observations[80].

2.3.2.3.4B: Prediction Step

The prediction step involves estimating the state vector and the error covariance matrix at the next time step, based on the current state estimate and error covariance matrix. From the state transition equation, the predicted state estimate $\hat{x}_{k|k-1}$ is derived by taking the expectation, assuming that the process noise w_{k-1} has zero mean. Therefore, the predicted state estimate is[80]:

$$\hat{x}_{k|k-1} = F_{k-1}\hat{x}_{k-1|k-1} + B_{k-1}u_{k-1} \tag{2.19}$$

Equation 2.19 shows how the predicted state is obtained by propagating the previous state through the state transition model and adding the effect of the control input. It is important to note that since the model being used only involves the position and velocity of a lung tumor, there is no control input present, so B and u are effectively zero for our implementation.

The predicted error covariance $P_{k|k-1}$ quantifies the uncertainty in the predicted state estimate. It is calculated by propagating the current error covariance through the state transition, while accounting for the process noise covariance[80]:

$$P_{k|k-1} = F_{k-1}P_{k-1|k-1}F_{k-1}^{T} + Q_{k-1} \tag{2.20}$$

This equation comes from the propagation of uncertainties through the linear model, where $P_{k-1|k-1}$ is the error covariance at the previous time step, and Q_{k-1} accounts for the added uncertainty due to process noise[80].

2.3.2.3.4C: Update Step

In the update step, the Kalman filter incorporates the new measurement to refine the predicted state estimate and error covariance matrix. The measurement residual (or innovation) y_k is the difference between the actual measurement z_k and the predicted measurement $H_k\hat{x}_{k|k-1}$[80]:

$$y_k = z_k - H_k\hat{x}_{k|k-1} \tag{2.21}$$

This equation represents the discrepancy between what is expected to be observed (predicted measurement) and what is actually observed (actual measurement).

The residual covariance S_k represents the uncertainty associated with the measurement residual. It is computed by considering the predicted error covariance propagated through the transformation matrix and adding the measurement noise covariance[80]:

$$S_k = H_k P_{k|k-1} H_k^T + R_k \tag{2.22}$$

The Kalman gain K_k determines how much trust should be placed in the new measurement versus the predicted state estimate. It is derived by minimizing the posterior error covariance matrix (post measurement update), ensuring the optimal trade-off between the predicted state estimate and the new measurement[80]:

$$K_k = P_{k|k-1} H_k^T S_k^{-1} \tag{2.23}$$

Using the Kalman gain, the state estimate $\hat{x}_{k|k}$ is updated by adjusting the predicted state estimate with the measurement residual[80]:

$$\hat{x}_{k|k} = \hat{x}_{k|k-1} + K_k y_k \tag{2.24}$$

Finally, the updated error covariance matrix $P_{k|k}$ reflects the reduced uncertainty in the state estimate after incorporating the measurement. It is calculated as[80]:

$$P_{k|k} = (I - K_k H_k) P_{k|k-1} \tag{2.25}$$

By recursively applying these prediction and update steps, the Kalman filter provides an efficient and optimal estimate of the system's state over time, effectively combining prior knowledge and new measurements to track the true state of the system in the presence of noise[80]. Figure 2.10 shows how these equations interact to iteratively build a series of state estimates.

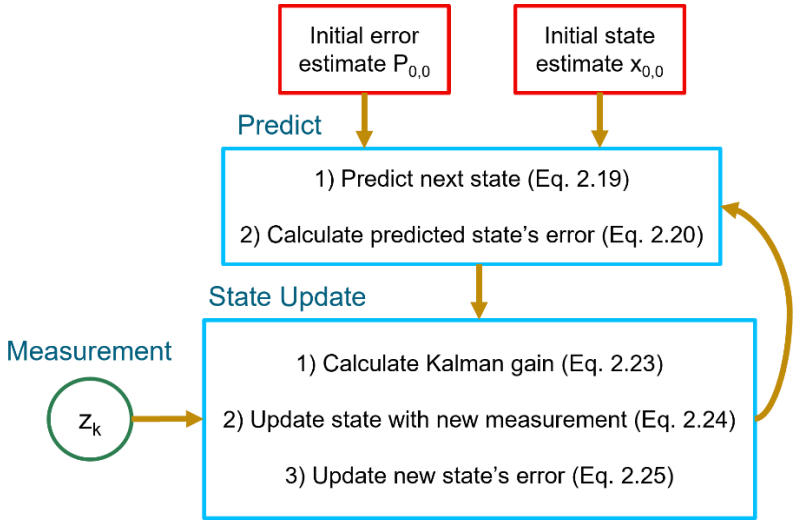

Figure 2.10: Kalman filter flowchart describing how equations are used to build a series of estimates based on dynamic model and sequential measurements.

2.3.2.3.4D: Implementation of Kalman Filter

The Kalman filter may be implemented as an alternative to the Gaussian PDF technique employed throughout Chapter 2. The vectors and matrices described in the previous sections must be redefined in the context of the ExacTrac imaging system and the 3D position of the moving lung tumor. First, the state vector x_k may be defined to be the 3D position and velocity of the lung tumor at a particular state k:

$$x_k = \begin{pmatrix} x \\ y \\ z \\ \dot{x} \\ \dot{y} \\ \dot{z} \end{pmatrix} \tag{2.26}$$

Next, the state transition matrix F, which describes how the state vector x_k changes from one iteration to the next, is defined using simple motion equations:

$$F = \begin{pmatrix} 1 & 0 & 0 & dt & 0 & 0 \\ 0 & 1 & 0 & 0 & dt & 0 \\ 0 & 0 & 1 & 0 & 0 & dt \\ 0 & 0 & 0 & 1 & 0 & 0 \\ 0 & 0 & 0 & 0 & 1 & 0 \\ 0 & 0 & 0 & 0 & 0 & 1 \end{pmatrix} \tag{2.27}$$

The measurement z_k was chosen to be the 2D imager measurement:

$$z_k = (x_{im} \quad y_{im} \quad \dot{x}_{im} \quad \dot{y}_{im}) \tag{2.28}$$

The process noise covariance Q, representing the uncertainty in the model or the system, was chosen to be the patient-specific motion covariance associated with the ground truth used throughout the manuscript[67]. In other words, Q remains consistent between Gaussian PDF and Kalman filter approaches, but the Kalman filter makes use of velocity covariances as well. The velocity at one point in time is taken as the difference between the current and previous position, divided by the time differential (i.e., 0.6 seconds). The first three rows and columns, the position-only covariance matrix, is also used in equation 2.9. Q is therefore the 6x6 matrix:

$$Q = \begin{pmatrix} var(x) & \cdots & cov(x, \dot{z}) \\ \vdots & \ddots & \vdots \\ cov(\dot{z}, x) & \cdots & var(\dot{z}) \end{pmatrix} \tag{2.29}$$

$$= \begin{pmatrix} 0.0695 & 0.0281 & 0.1929 & 0.0684 & 0.0263 & 0.8281 \\ 0.0281 & 0.0273 & 0.1734 & 0.0208 & 0.0286 & 0.3721 \\ 0.1929 & 0.1734 & 19.3994 & -0.8713 & -0.2961 & 5.2248 \\ 0.0684 & 0.0208 & -0.8713 & 0.2285 & 0.0786 & -0.0335 \\ 0.0263 & 0.0286 & -0.2961 & 0.0786 & 0.0949 & 0.1455 \\ 0.8281 & 0.3721 & 5.2248 & -0.0335 & 0.1455 & 19.8045 \end{pmatrix}$$

Distances and speeds are given in mm and mm/sec. While Q does remain constant, it will continuously update the predicted state error covariance $P_{k|k-1}$ (which is initialized to zero) on each iteration, as per equation 2.20.

The measurement noise covariance matrix R, representing the uncertainty in measurements, was built using the covariance matrix of the standard deviations of pixel positions and velocities for each imaging tube. Standard deviations were calculated from

differences between template matching estimates and the ground truth for stereoscopic measurements of the entire breathing cycle, effectively giving a value representing uncertainty in template matching. This resulted in a 4x4 matrix for each tube of the form:

$$R = \begin{pmatrix} var(\sigma_{x_{im}}) & \cdots & cov(\sigma_{x_{im}}, \sigma_{\dot{y}_{im}}) \\ \vdots & \ddots & \vdots \\ cov(\sigma_{\dot{y}_{im}}, \sigma_{x_{im}}) & \cdots & var(\sigma_{\dot{y}_{im}}) \end{pmatrix} \tag{2.30}$$

The matrix R is constant for all iterations, as measurement uncertainty is not expected to change for the duration of the tracking, since it is mostly associated with template matching accuracy. For dual energy, the values for the R matrix for both tubes are:

$$R_A = \begin{pmatrix} 0.4720 & 0.4081 & 0.7564 & 0.6685 \\ 0.4081 & 0.3528 & 0.6540 & 0.5780 \\ 0.7564 & 0.6540 & 1.2122 & 1.0713 \\ 0.6685 & 0.5780 & 1.0713 & 0.9467 \end{pmatrix} \tag{2.31}$$

$$R_B = \begin{pmatrix} 0.3576 & 0.2518 & 0.5490 & 0.4222 \\ 0.2518 & 0.1772 & 0.3865 & 0.2972 \\ 0.5490 & 0.3865 & 0.8427 & 0.6481 \\ 0.4222 & 0.2972 & 0.6481 & 0.4984 \end{pmatrix} \tag{2.32}$$

Once again, distances and speeds are given in mm and mm/sec. Like Q, R remains constant for our implementation, but will update the residual covariance S_k on each iteration, as per equation 2.22.

The last parameter that needed to be defined for the Kalman filter is the transformation matrix H. This matrix transforms a 3D state (x, y, z, $\dot{x}$, $\dot{y}$, $\dot{z}$) prediction into a 2D measurement domain for each tube t knowing the ExacTrac geometry. For this implementation, H must translate 3D phantom coordinates into 2D x-ray imager screen coordinates, making use of room geometry, rotations, and coordinate system transformations between lab and phantom:

$$H_t = \frac{SDD^3}{SAD^2} \begin{pmatrix} 1 & 0 & 0 \\ 0 & 0 & -1 \end{pmatrix} \frac{R_x^T R_y^T}{n \cdot v_{lab} - SAD} + \frac{c(t)^T}{v_{ph}} \tag{2.33}$$

Several of these values are tube dependent. SDD (source-detector distance) and SAD (source-axis/isocenter distance) describe the room geometry, being 343.5 cm and 218.5 cm respectively[70]. R_x and R_y are rotation matrices that rotate from the room coordinates to each imaging plane t and are shown in equation 2.5.

n is the vector normal to the imager plane:

$$n = [-\cos(\theta)\cos(\phi) \quad -\sin(\theta)\cos(\phi) \quad -\sin(\phi)] \tag{2.34}$$

For ExacTrac imaging panels A and B, $\theta_A = \theta_B = 48°$, $\phi_A = -45°$, and $\phi_B = 45°$.

v_{ph} is the input 3D phantom coordinate that is to be converted to a 2D position on either imager plane t:

$$v_{ph} = [x_{ph} \quad y_{ph} \quad z_{ph}] \tag{2.35}$$

v_{lab} is the same 3D point, converted to lab coordinates:

$$v_{lab} = [-z_{ph} \quad x_{ph} \quad -y_{ph}] \tag{2.36}$$

Finally, c(t) is the transformation matrix that converts the central axes to the ExacTrac viewer origin on the corner of the image. position of the ExacTrac system. These are the 2D points on either imager that correspond to a projection from the 3D isocenter position:

$$c = \begin{pmatrix}[243,256]\\[235,260]\end{pmatrix} \tag{2.37}$$

These values are converted from pixels to distance measurements by multiplying them by the pixel size of 0.397 mm/px.

The resulting transformation matrix H_t has dimensions of 4x3 but is padded with zeros on the off diagonals into a matrix of size 4x6, such that it may be used for velocity transformations as well. As an example, the following is the first iteration of H for tube A with

dual energy:

$$H_A = \begin{pmatrix} 42.2518 & 2.8875 & -1.8384 & 0 & 0 & 0 \\ 49.1965 & 0 & -2.7475 & 0 & 0 & 0 \\ 0 & 0 & 0 & 42.2518 & 2.8875 & -1.8384 \\ 0 & 0 & 0 & 49.1965 & 0 & -2.7475 \end{pmatrix} \quad (2.38)$$

2.4: Results

2.4.1: PDF Results

Figure 2.11 shows examples of DE and conventional SE images for the 19.1 mm tumor from both stereoscopic views for one frame. From the perspective of Tube A, the moving tumor is often behind a rib. Likewise, for Tube B, the tumor is obscured for its entire trajectory by spinal vertebrae. The dual energy imaging, as shown in the bottom two images, allows for suppression of bone contrast in the region surrounding the tumor. As described in section 2.3.2.3.1, the stereoscopic imaging system results in images created by beams passing through the phantom at oblique incident angles (polar angle 48°, and azimuthal angles ± 45°).

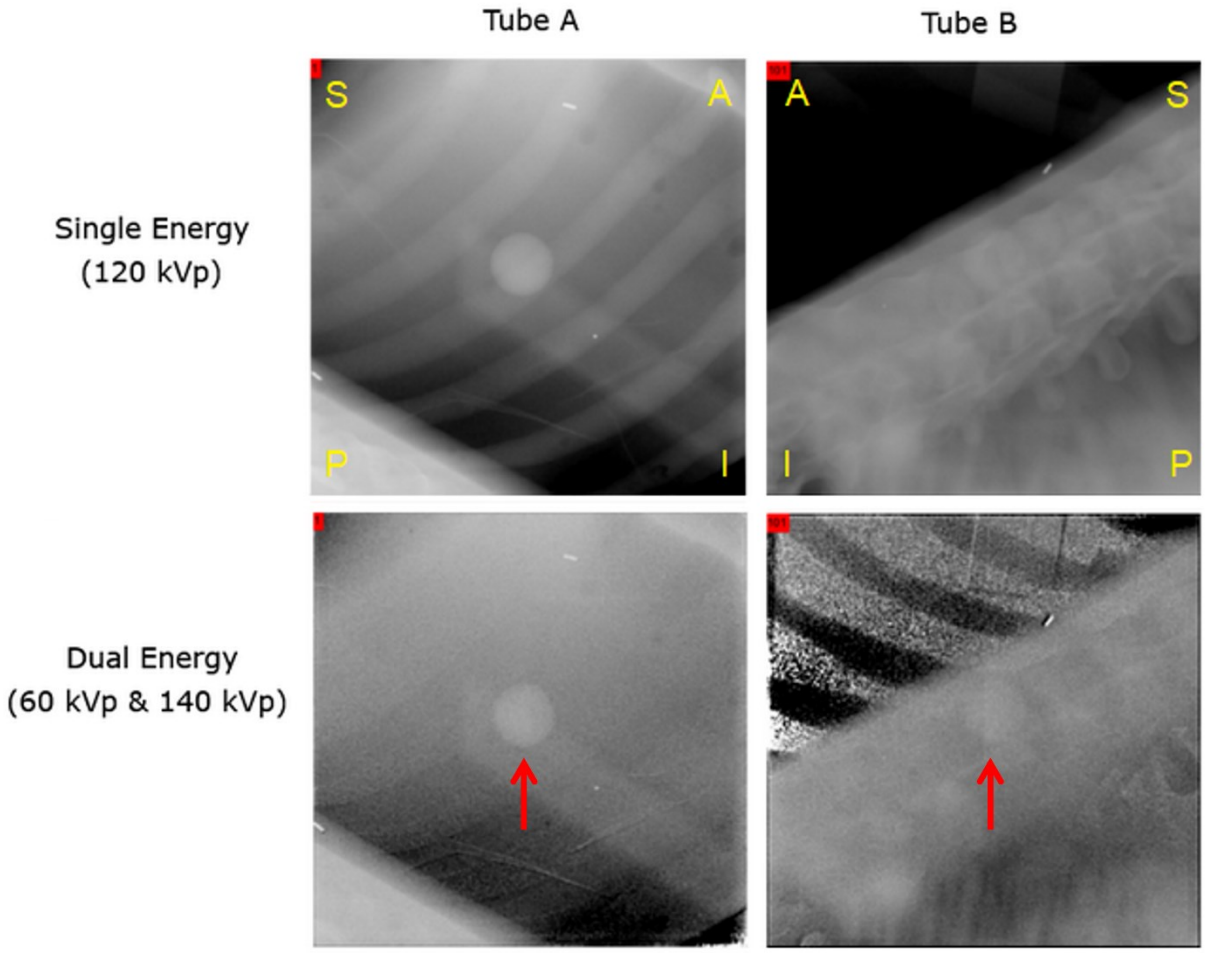

Figure 2.11: Dual energy and single energy images of a 19.1 mm tumor, as seen from both stereoscopic views. Tube A is the view where the tumor is blocked by the rib, and Tube B is the view where the tumor is blocked by the spinal cord. A/P and S/I represent the anterior-posterior and superior-inferior directions on the images.

Figure 2.12 demonstrates results of the 3D tumor localization for both single and dual energy imaging techniques for the 12.7 mm tumor. Similar results were obtained for other tumor sizes. The 3D localizations are plotted separately in left-right lateral (LR), anterior-posterior (AP), and superior-inferior (SI) directions.

Figure 2.13a illustrates the localization success rates in the SI direction with respect to tumor size for both dual energy and single energy techniques. The corresponding tumor localization accuracy and precision are demonstrated in Figure 2.13b.

For the largest tumor size (25.4 mm), the localization success rate was 100% for the

stereoscopic regions when both imaging views were available for both SE and DE techniques (Fig. 2.7a). The SE success rate decreased to as low as 50% for the smallest tumor size (6.4 mm), while the DE success rate did not fall below 92% across all tumor sizes, indicating superior results than the SE technique.

In the monoscopic regions of Tube A, where the tumor was blocked by the ribs, the PDF estimate showed promising results, having 100% localization success rate across almost all tumor sizes for both DE and SE techniques. The only exception was the SE technique for the smallest tumor of 6.4 mm, having a localization success rate of only 57%. In the monoscopic regions of Tube B, where the tumor was blocked by the spinal vertebrae, the DE technique showed a superior performance compared to the SE technique for all tumor sizes. The success rate decreased for both DE and SE for smaller tumors, with significant improvement being shown for the second smallest tumor size (12.7 mm), having a DE success rate of 93%, compared to 73% for the SE technique. Monoscopic localization in region B showed a 0% success rate for the smallest tumor (6.4 mm) for SE, while DE had only a modest improvement up to 7%. In terms of the accuracy of the localization (Figure 2.7b), the stereoscopic localization error mostly remained around 1 mm, having a range of [0.33-2.21], while the monoscopic PDF localizations for either tube views were larger at around 1-2 mm for both SE and DE techniques. Because of the 0% localization success in Tube B for SE for the smallest tumor size (6.4 mm), no error bar was calculated.

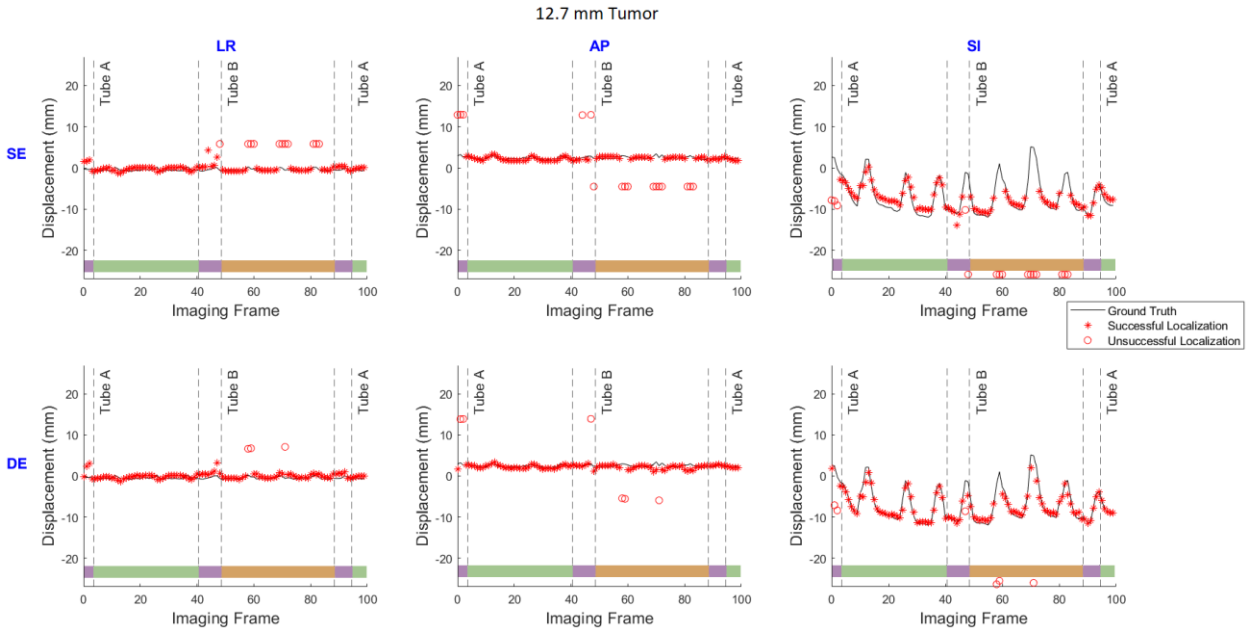

Figure 2.12: Estimated 3D tumor localizations using single and dual energy techniques for the 12.7 mm tumor. Asterisks indicate successful localizations (error < 5 mm), while empty circles indicate those that were unsuccessful. The color bars at the bottom of each graph label stereoscopic regions (purple), and monoscopic regions seen by Tubes A or B (green or orange respectively) as per Figure 2.3.

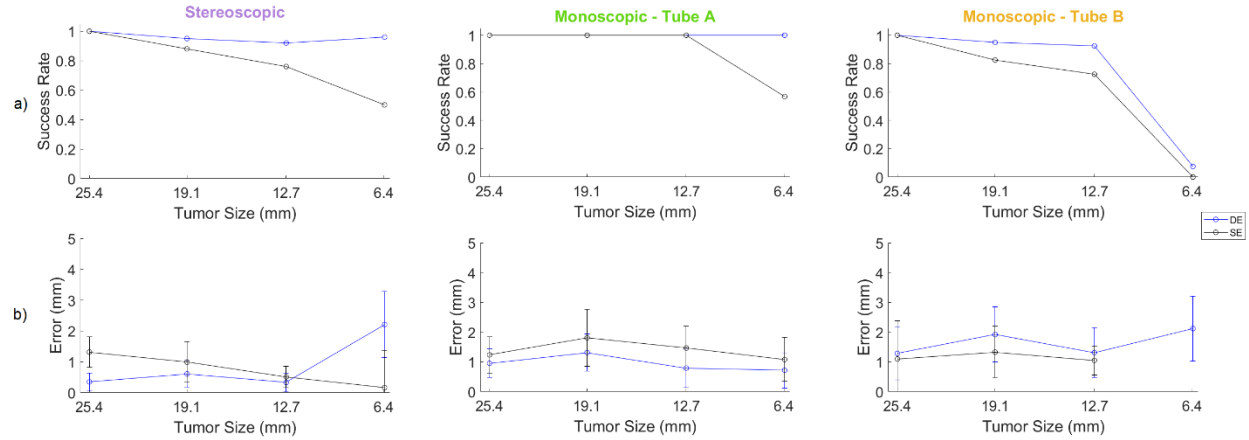

Figure 2.13: (a) Success rate and (b) error (accuracy ± precision) of stereoscopic localization, and monoscopic PDF estimates for each imaging view, with respect to tumor size, in the SI direction. Error bars are one standard deviation.

2.4.2: Epipolar Results

Using the algorithm in section 2.3.2.3.2, preliminary tumor localization results were

obtained for the anthropomorphic lung phantom using the real images discussed throughout this chapter. Figure 2.14 shows the epipolar constraint applied for the DE images on a half inch tumor.

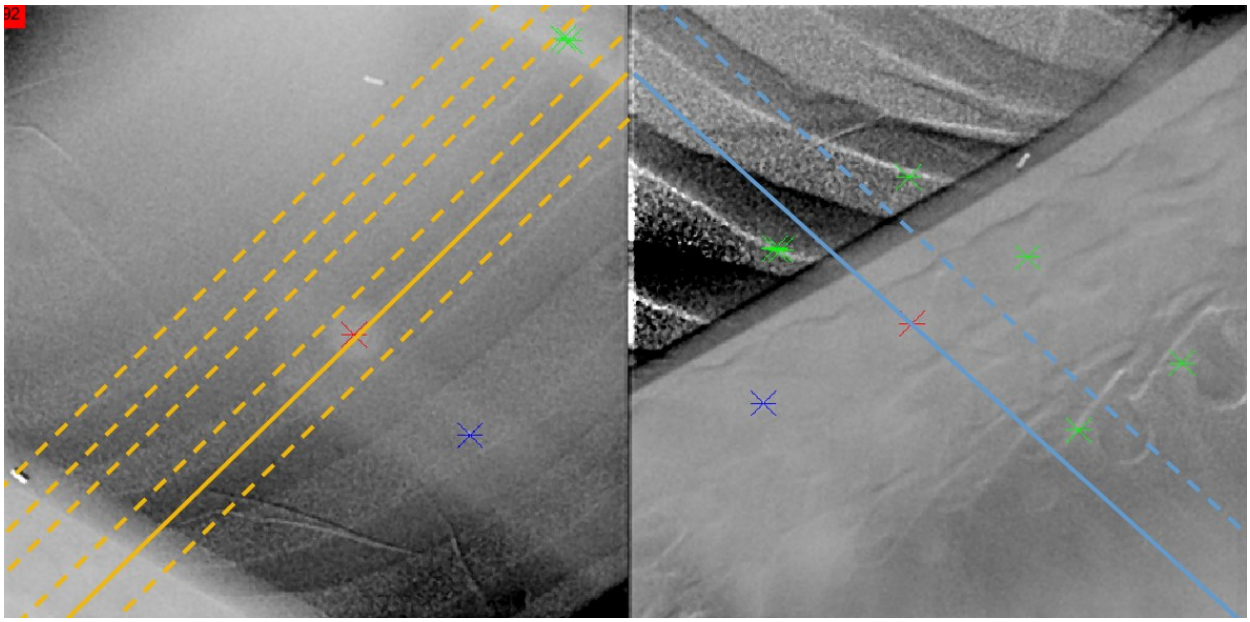

Figure 2.14: Epipolar points shown in green in the right image forming an epiline corresponding to the template matched red marker on the left image. The right image red marker corresponds to the point on the epiline with the maximum combined correlation score. It should be noted that the blue marker is irrelevant for this experiment.

Figure 2.15 shows the preliminary results of the epipolar algorithm, compared to those without the use of the epipolar constraint.

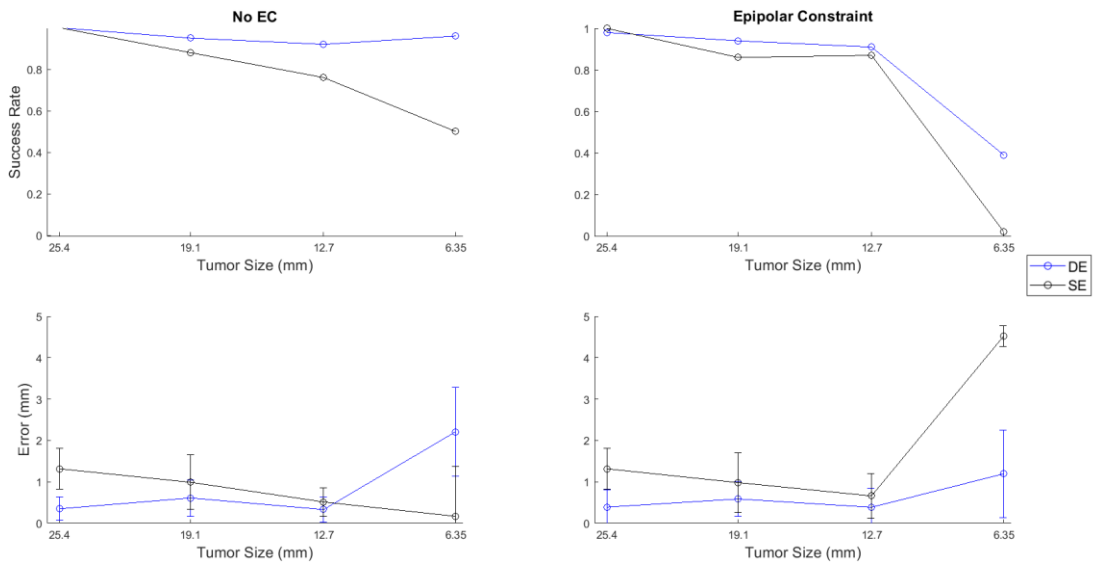

Figure 2.15: Success rate and error (accuracy ± precision) of stereoscopic localization, with and without the use of the epipolar constraint (EC), with respect to tumor size, in the SI direction. Error bars are one standard deviation.

2.4.3: Preliminary Kalman Results

The Kalman implementation yielded results demonstrated in Figure 2.16, which displays 2D imager pixel values (x and y) with respect to time. Similar to the Gaussian PDF implementation, the results graph is divided into regions corresponding to whether it is a stereoscopic or a monoscopic (tube A or tube B) situation. The graphs show the ground truth values (as projected from the ground truth 3D position on to each of the 2D imagers), as well as the 2D positions predicted from template matching with dual energy, along with the 2D positions predicted by the Kalman filter approach.

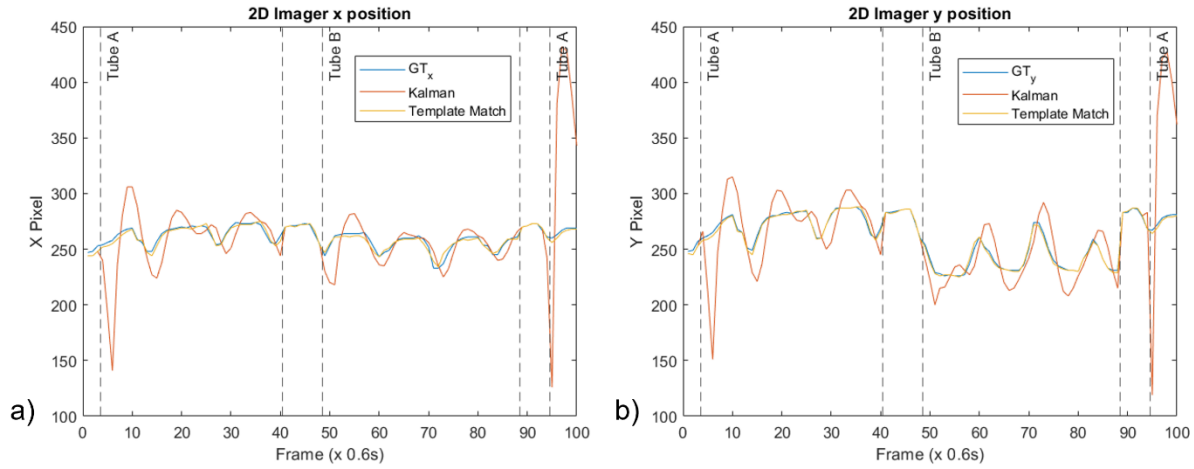

Figure 2.16: 2D imager (a) x and (b) y pixel coordinates as determined by ground truth projection, Kalman filter estimations, and template matching with dual energy.

2.5: Discussion

This study develops a real-time markerless lung tumor monitoring technique with dual energy imaging capability using a clinical room-mounted kV x-ray imaging system. We addressed a significant issue associated with real-time imaging during treatment using the imaging system, i.e., the blocking of an x-ray beam by the rotating linac gantry. This problem was addressed by applying a Gaussian probability density function approach to calculate a 3D position estimate using only limited 2D information from single x-ray view based on patient-specific motion covariances of the lung tumor.

As per Figure 2.13, dual energy consistently demonstrated improved success rates throughout all tumor sizes for both stereoscopic and monoscopic imaging techniques. Stereoscopic localization of the tumor over its trajectory using dual-energy technique yielded near-perfect success rates for all tumor sizes. Single energy success rates, however, demonstrated a decreasing trend with decreasing tumor size. As expected, this illustrates that suppressing bone contrast in situations where the lung tumors are obstructed by bone has a favorable effect on the tumor localization estimates for markerless tracking. This finding is consistent with previous dual energy studies using non-stereoscopic systems[50,51,53,82]. The accuracy and precision of the stereoscopic localization reveals no noticeable trend for the three larger tumor sizes, having errors on the order of ~1 mm, while the largest uncertainties were

observed for the 6.4 mm tumor. The significant overlap of the error bars indicates there is little to no difference in localization errors between dual and single energy approaches for stereoscopic imaging. This suggests that dual energy imaging reduces the number of image frames with large errors in tumor localization (Figures 2.12, 2.13), but has little effect in reducing the smaller localization errors brought on by imperfect bone tissue cancellation or errors in template matching.

Monoscopic localizations were categorized based on tumor obstruction by the rib bone (Tube A) or the spine (Tube B). Tube A achieved 100% success rates for both dual and single energy imaging for the three largest tumors. For the smallest tumor (6.4 mm), dual energy maintained 100% success, while single energy localization dropped to 57%. Although localization errors were larger than stereoscopic results, no significant differences were observed between dual and single energy techniques for Tube A. In contrast, Tube B showed that dual energy provided superior localization over single energy, particularly for smaller tumors, due to greater interference from thicker bone. The localization errors generally increased with decreasing tumor size, which matches the expectation of difficulties of successful localization of smaller tumors. These findings highlight the potential of dual energy imaging to enhance tumor visibility and accuracy, especially in challenging anatomical contexts.

The localization of the smallest tumor (6.4 mm) was the least successful and generally with the highest errors. This is likely due to this tumor approaching a size comparable to neighboring (and overlapping) anatomical features such as the vertebrae along the phantom's spine. When the tumor overlaps with such features in Tube B, the signal from the cross-correlation algorithm is not as strong, leading to a higher likelihood of incorrect localization. Considering that the GTV size in lung patients are typically larger than 1 cm due to accuracy limitation with small field dosimetry[83], the lack of detectability for the 6.4 mm tumor size may not in most cases pose a significant clinical problem.

Interestingly, the use of the epipolar constraint seemed to have little if any effect on the DE measurements for the three largest tumor sizes (differences of 1%), while having a detrimental effect on the smallest size, reducing the localization success from 96% to 39%. There are some improvements in the SE case, most notably for the 12.7 mm tumor, having a

successful localization rate increase of about 10%. However, there is still a major decrease for the smallest tumor size. This is counterintuitive to what was expected, since ideally the epipolar restriction should have increased success rates across the board or would maintain similar results as seen for some of the larger tumor sizes. A potential explanation for this could be that since epilines cross over regions of high pixel intensity, there are more cases that misidentify such regions as tumors, especially considering how the number of epilines seems to increase with decreasing tumor size. Further investigation into the implementation and analysis of the epipolar constraint for tumor localization is necessary. Potential solutions could include adjusting epipolar constraint parameters such as median filter size, and the thresholds C_{thresh} and δ.

Due to the fixed geometry of the room-mounted stereoscopic imaging system, tumor obstructions would be present throughout the entire treatment. This differs from tumor tracking procedures using on-board imaging introduced in previous studies[27,53] where the imaging system revolves around the target volume and different bone obstructions occur at different parts of the patient's breathing pattern. Haytmiradov's study demonstrates that the poorest tracking accuracy occurs when the tumor is obstructed by the spine[53]. In this study, 100% of the phases for the Tube B view dealt with spinal occlusion, while for Haytmiradov et al., it occurred one third of the time. Similar to this study, Haytmiradov et al. also demonstrated that the use of DE imaging improves the localization success rate when dealing with spinal overlap as compared to SE imaging.

Real-time imaging adds dose to the PTV and surrounding OARs which cannot be ignored. Abeywardhana et al. quantified the patient-specific imaging dose for ExacTrac monoscopic / stereoscopic real-time kV image guidance received by lung and prostate patients[84]. With a validated Monte Carlo model using DOSEXYZnrc[85], they found that bone and skin received the highest imaging dose, with larger patients having received more dose in these regions than smaller ones. For lung patients, the dose delivered to 2% of organ volume (D2) of the bone and skin maximized at 4.30% and 1.98% of the prescription dose respectively. Additional imaging dose to the PTV itself was reported to be 2.42% of the prescription. These values are below the AAPM-TG-180 recommended imaging dose threshold of 5%, beyond which imaging dose must be accounted for during the treatment planning process[86]. In a follow up study quantifying how imaging doses could affect OAR constraints in treatment planning,

Abeywardhana investigated the effect of additional dose from monoscopic / stereoscopic real-time tumor monitoring in 30 lung SBRT patients with a total of 565 PTV and OAR constraints[87]. However, there was only one instance out of those 565 constraints (0.2% of cases) that led to an OAR dose constraint failure when adding imaging dose to treatment dose, in which the imaging dose was 1.9% of the prescription. In all cases, the real-time imaging dose did not exceed the recommended TG-180 threshold, suggesting that additional real-time imaging dose may not be clinically significant. Moreover, a reduction of PTV margins via real-time imaging (e.g., by minimizing ITV margins to only residual motion) could significantly reduce nearby OAR treatment doses, a fact which was not accounted for in the above imaging dose studies.

Montanaro et al. examined a variety of 2D-3D inference methods in combination with on-board single energy 2D kV imaging systems with the goal of evaluating real-time target tracking accuracies[79]. Similar to this study, they investigated the Gaussian PDF method, which models the probability density of the target[88]. Additionally, they examined arbitrary-shape PDFs (A-PDF), which represent the 3D target's probability density as a superposition of exponential functions based on previously observed positions[89]. Furthermore, they explored interdimensional correlation (IDC), which leverages linear dependencies between LR, AP, and SI motions, exploiting the unambiguity of the SI component measured by the kV imager[90]. Finally, they studied the Kalman filter, which combines measurements with a model based on prior knowledge to estimate system evolution over time[80,91]. Montanaro et al. found that for lung patients, Gaussian PDF was the most accurate method, followed by the Kalman filter, IDC, and A-PDF. Longer temporal windows (120 - 140 s) were recommended for PDF-based methods, while shorter ones (60 s) were advantageous for the Kalman filter to capture the most recent motion patterns. Future work building on this study may potentially examine the use of these other techniques to investigate the potential improvements of the localization estimates with the addition of dual energy technique.

Similar to PDF, Kalman filter was only applied in the defined regions where either x-ray tube A or B has the sole point of view of the tumor due to the rotating gantry. In the most ideal case, the Kalman prediction would quickly converge to match the ground truth within a few iterations. This pattern is seen to some extent for the x and y coordinates in both tubes. However, since the predictions are being updated for more than 30 seconds, they should ideally be much

closer to the ground truth. This indicates an issue with implementation of the Kalman filter. It is a strong possibility that the ExacTrac's imaging frequency (1.67 Hz) is not sufficient for the Kalman filter to be a suitable estimator, as lung tumor position can vary widely within a short window of time. Higher imaging frequencies on the order of 10 Hz may be necessary to achieve more promising results[92]. Future efforts to implement a Kalman filter model for the ExacTrac system should involve modifying various matrices and vectors. This may include incorporating acceleration into the motion model and re-evaluating the transformation matrix H used for converting between 3D and 2D coordinates. One key issue with the current implementation is the presence of a squared magnification factor (SDD/SAD) in the matrix H. This factor is problematic because it scales a distance, which should not be squared as it represents a geometrical aspect rather than an area. Despite this, the existing approach has yielded better results compared to other attempts (this is the only implementation that reasonably predicts 2D coordinates as shown in Figure 2.16). Nonetheless, future work will need to thoroughly re-examine and adjust the H matrix.

The methodology and results of DE imaging in this study may also be applied to other stereoscopic image guidance systems such as CyberKnife[54,55], Vero system[93], and SyncTracX[56], where frequent blocking of one view is less of a concern. Combining the stereoscopic and monoscopic techniques described throughout this paper, the clinical room-mounted image guided system could be capable of real-time lung tumor monitoring with the improved success rate brought on by dual energy imaging technique. This capability needs to be evaluated on lung cancer patients in clinical settings to facilitate clinical adaptation.

2.6: Conclusion

A real-time markerless imaging system was developed, combining stereoscopic and monoscopic tumor tracking techniques for lung tumor patients. Integration of dual energy significantly improves tumor localization success rates compared to the conventional single energy approach, particularly for smaller tumors. Probability Density Functions (PDFs) provide a promising approach to monoscopic estimates when the room-mounted stereoscopic imaging system is partially blocked by the rotating gantry. This study indicates the potential for accurate real-time markerless tumor tracking, which could improve precision radiotherapy by removing the need for a large ITV margin and thus minimizing treatment of healthy tissues.

Chapter 3: Conclusion

The work shown so far in this thesis introduced a real-time, markerless lung tumor monitoring technique utilizing DE imaging developed for a room-mounted clinical kV x-ray imaging system. A notable challenge in this approach was overcoming the issue of x-ray beam obstruction by the rotating linac gantry during treatment. To address this, a Gaussian PDF method to estimate 3D tumor positions from limited 2D x-ray views was used, accounting for patient-specific tumor motion covariances. This approach effectively mitigated the imager blockage issue, enhancing real-time tracking capabilities.

The findings demonstrate that DE imaging considerably improves localization success rates for lung tumors, especially smaller ones, compared to SE techniques. DE imaging demonstrated near-perfect localization accuracy for various tumor sizes using stereoscopic techniques, while SE methods displayed a decline in success rates as tumor size decreased. This enhancement in accuracy is attributed to the DE technique's ability to suppress bone contrast, which is particularly beneficial when tumors are obstructed by bone structures. Despite this improvement, stereoscopic localization errors remained consistent across larger tumor sizes, with notable inaccuracies for the smallest tumor (6.4 mm). This suggests that while DE imaging helps reduce large localization errors, it has a limited impact on smaller errors due to residual bone tissue interference or template matching issues.

In addition to stereoscopic imaging, monoscopic localization was analyzed based on whether tumors were obstructed by rib bones or the spine (this differed based on the angle of the ExacTrac beam). DE imaging provided superior results for smaller tumors when obstructions were from thicker bone structures, such as the spine. This underscores the potential of DE imaging to enhance tumor visibility and accuracy in challenging anatomical contexts. Notably, for the smallest tumors, DE consistently outperformed SE imaging, particularly in scenarios with significant bone interference. Although real-time imaging introduces additional radiation dose to the PTV and surrounding organs, this dose remains below recommended safety thresholds. Moreover, the improved precision in tumor localization can lead to smaller PTV margins, which in turn reduces the radiation exposure to healthy tissues at a much bigger scale than the imaging dose.

It was concluded that DE imaging technique, combined with stereoscopic and monoscopic monitoring, holds significant promise for improving real-time tumor tracking, potentially facilitating more precise radiotherapy by minimizing the need for large ITV margins and thus reducing exposure to healthy tissues. The remaining sections of this thesis will cover future potential research avenues that could be pursued as a logical continuation to the results presented in the previous two chapters.

3.1: Effect of Tumor Size, Shape, and Density on Detectability and Localization

Throughout the work done for this thesis, spherical tumors of uniform density were used to model lung tumors. Realistically, this will rarely be the case, as tumors will present themselves in many unique shapes, sizes, and densities (see Fig. 3.1).

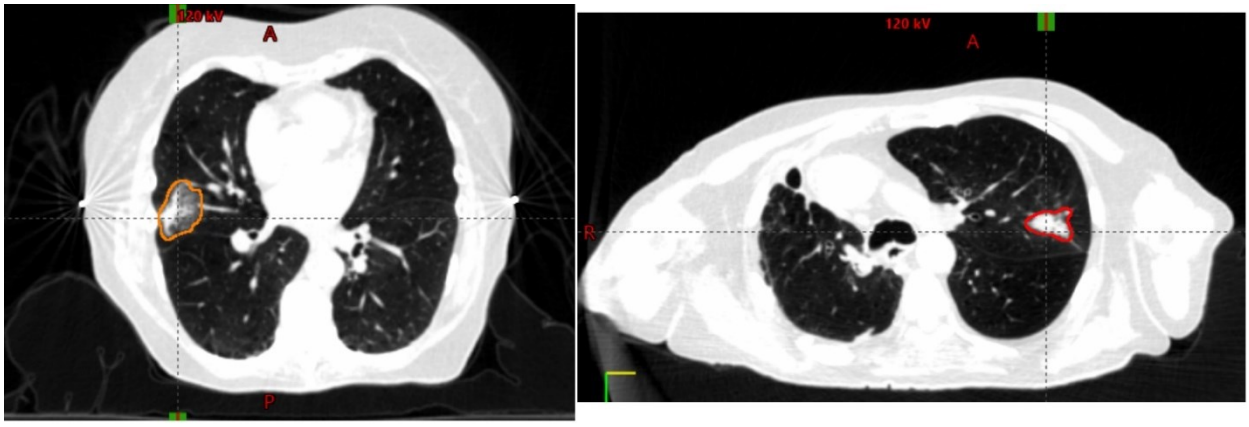

Figure 3.1: Two different lung patients showing tumors of differing sizes, shapes, and densities. Notably, the patient on the left has lower tumor density than the one on the right. Both images are shown using the same "lung" window/level display setting.

Non-spherical tumors introduce complexity in imaging and detection due to their irregular shapes. Traditional spherical models fail to capture the nuances of these shapes, leading to potential inaccuracies in tumor size estimation and localization. Realistic tumor sizes vary widely, but it is essential to account for these variations when designing and interpreting imaging studies. More realistic scenarios can be modeled and created utilizing 3D printing technology to create practical tumor models. Additionally, the dynamic nature of tumors during the breathing cycle, which can be captured using 4DCT, also may lead to tumor shape changes and affect imaging results. Tumor density also plays a critical role, as denser tumors can be more

easily distinguished from surrounding tissues, whereas less dense tumors might be more challenging to detect. Template matching algorithms consider all the above effects that lead to changing the state of the tumor, and certain templates may be assigned depending on the situation. For example, to capture changes in the tumor shape during breathing cycle, three tumor shapes from three phases of 4DCT breathing cycles (0%, 50%, and 90%) can be calculated from the corresponding three DRRs, which can then be used during the template matching for tumor localization.

3.2: Challenge of small object detectability using x-ray imaging

Localization errors pose significant challenges in tumor imaging, particularly for smaller tumors. The Rose model, introduced in section 1.4.4, describes the relationship between object size, contrast, and noise, indicating that smaller tumors are harder to detect due to lower signal-to-noise ratios. This model, which is primarily applicable to SE imaging, assumes detectability arises solely from quantum noise. It assumes a uniform tumor in a uniform background and an ideal detector ignoring electronic noise and adjacent pixel correlation due to loss of spatial resolution in the detector. Anatomical noise, which DE imaging aims to mitigate, significantly impacts detectability. Inhomogeneities in lung tissue densities add to this challenge, as real patients present more complex textures compared to uniform phantoms used in simulations, with factors such as bone overlap, motion artifacts, and minor anatomical features further complicating detection. While there is no direct implementation of the Rose Model for multiple energies, object detectability fundamentals could be investigated for DE images simulated from two SE images using cascaded modeling[14]. DE imaging offers significant advantages in reducing anatomical noise and improving detectability, but further considerations are necessary for the diverse and dynamic nature of tumors in clinical settings.

3.3: Clinical implementation of this thesis

This thesis presents feasibility and preliminary results on the markerless monitoring of lung tumors using DE imaging with a room-mounted imaging system, while considering the existence of monoscopic scenarios due to gantry rotation. The next logical step would be to investigate how the system may be implemented in the clinic. This section explores the integration of various technological advancements, including multileaf collimator (MLC) tracking, fast kVp switching, and adaptive weighting factor updating, to implement tumor

tracking.

The adoption of MLC tracking in radiotherapy is a significant development for real-time tumor monitoring. As outlined in TG-264[94], the implementation of MLC tracking involves addressing various uncertainties and ensuring that the technology meets stringent clinical requirements. The integration of MLC tracking aims to reduce the CTV to PTV margins, potentially enhancing treatment precision. However, overly tight margins may lead to adverse outcomes if not supported by accurate target definition and motion tracking[95].

A comprehensive MLC tracking system (Fig. 3.2) must account for uncertainties such as the accuracy of motion surrogates, target deformation, and tracking errors. These uncertainties necessitate rigorous validation and quality assurance protocols to ensure the system's safety and efficacy. The system's design should include real-time localization and adaptation capabilities, with automated checks for connectivity, motion range, and dose delivery. Adherence to TG-264 guidelines is essential for successful clinical integration, as it provides a framework for safe implementation and continuous monitoring[94]. Compliance with these guidelines is required for regulatory approval and successful clinical integration.

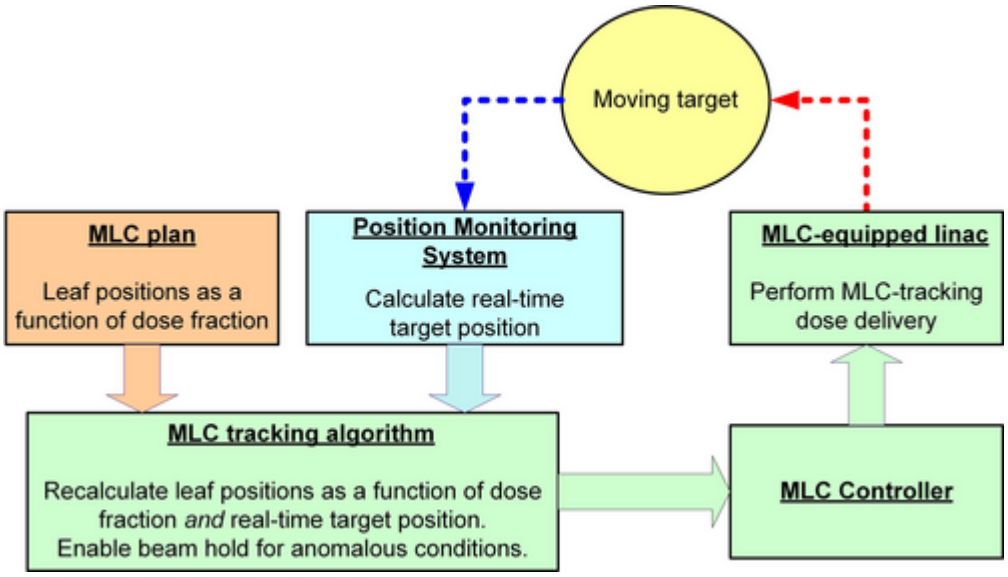

Figure 3.2: An example multileaf collimator (MLC) tracking workflow. The work of this thesis would be implemented into the blue-colored module "Position Monitoring System" to calculate the real-time target position.[94]

Fast kVp switching is a technique involves alternating between high and low energy x-ray beams at a rapid frame rate, capturing images that are then combined to create DE images. Although due to hardware limitation, the experimental setup performed during this thesis could not utilize fast kVp switching and required separate experiments for each kVp setting, future implementations in clinical settings would benefit significantly from this capability. Fast kVp switching minimizes motion artifacts and enhances temporal resolution by capturing dual-energy images almost simultaneously. This advancement is particularly valuable for tracking dynamic structures like the lungs, which move with respiration. Implementing this technology in clinical practice would require utilization of hardware and software configurations to achieve high frame rates and accurate image fusion[53].

Adaptive and automated weighting factor updating is another critical aspect of generating DE imaging in real-time for clinical use. Studies[96,97] have highlighted the importance of automated algorithms in selecting optimal weighting factors to enhance image quality and reduce artifacts. These algorithms adaptively adjust weighting factors based on imaging conditions and target characteristics, streamlining the workflow and minimizing manual intervention. Automated weighting factor selection allows real-time DE image calculation and improves contrast and reduces noise, making it feasible for routine clinical practice. This technology ensures that the imaging system continuously adapts to varying patient conditions and imaging parameters, enhancing the accuracy of tumor tracking and localization.

To transition from experimental setups to clinical practice, designing and conducting initial clinical trials is essential. These trials should focus on evaluating the feasibility, safety, and efficacy of the markerless tumor tracking system in a controlled environment. Key endpoints for these trials include feasibility of real-time DE imaging, the accuracy of tumor localization, and the system's ability to adapt to respiratory motion. Involving a diverse patient population with varying tumor sizes and shapes will provide comprehensive data on the system's performance. Clinical trials will also help identify any potential challenges and refine the system before broader clinical adoption.

The ground truth positions used for this thesis[67] was also used to construct the motion covariance-based PDF. In a realistic scenario, the true position of the lung tumor would not be

explicitly known. The PDF would therefore need to be constructed based on 4DCT data or using pre-treatment readings of surface marker.

The integration of DE imaging into the clinic holds the potential to have a significant impact on lung tumor tracking. The transition from experimental setups to clinical practice will require careful planning, robust validation, and ongoing evaluation to ensure the technology's effectiveness and safety.

3.4: Final Remarks

This thesis presented a dual-energy markerless imaging technique aimed at monitoring lung tumor motion using a clinical room-mounted x-ray imaging system in real-time. The introductory chapter laid the groundwork by discussing the fundamental principles of x-ray production and interactions, along with a comprehensive overview of imaging systems, including x-ray tubes and detectors. Additionally, the integration of dual-energy imaging in radiotherapy was examined, highlighting its potential to improve tumor localization and treatment delivery.

The core of this thesis presented the novel imaging technique in the form of a submitted research manuscript. This research addressed the significant challenge posed by x-ray beam obstruction due to rotating gantries in room-mounted stereoscopic imaging systems. A Gaussian probability density function (PDF) approach was employed to estimate the 3D position of lung tumors using limited 2D information from single x-ray views, aiming to enhance localization accuracy. The findings indicated that DE imaging improves tumor monitoring success rates compared to conventional SE imaging. Additionally, the integration and preliminary results of Kalman filtering techniques and epipolar constraints were included alongside the contents of the manuscript.

The third chapter extended the discussion to the clinical application of the developed system, incorporating various technological advancements and practical considerations. It discussed the implementation of MLC tracking, the application of fast kVp switching for practical real-time imaging, and the optimization of adaptive and automated weighting factors. Additionally, it explored aspects such as the effect of tumor size, shape, and density on

detectability and tracking performance.

In summary, the thesis thoroughly addressed the integration of real-time tumor tracking and dual energy imaging for lung radiotherapy. The research provides a robust foundation for future developments and implementations in the field, aiming to improve patient outcomes in radiotherapy.

Bibliography

1. Bushberg JT, Seibert JA, Leidholdt EM, Boone JM. *The Essential Physics of Medical Imaging*. 3rd ed., International ed. LWW; 2011.

2. Huda W. *Review of Radiologic Physics*. 3rd ed. Lippincott Williams & Wilkins; 2010.

3. Khan FM. *The Physics of Radiation Therapy*. 3rd ed. Lippincott Williams & Wilkins; 2003.

4. Kuhlman JE, Collins J, Brooks GN, Yandow DR, Broderick LS. Dual-energy subtraction chest radiography: what to look for beyond calcified nodules. *Radiogr Rev Publ Radiol Soc N Am Inc*. 2006;26(1):79-92. doi:10.1148/rg.261055034

5. Rebuffel V, Dinten JM. Dual-energy X-ray imaging: benefits and limits. *Insight - Non-Destr Test Cond Monit*. 2007;49(10):589-594. doi:10.1784/insi.2007.49.10.589

6. Vock P, Szucs-Farkas Z. Dual energy subtraction: principles and clinical applications. *Eur J Radiol*. 2009;72(2):231-237. doi:10.1016/j.ejrad.2009.03.046

7. MacMahon H, Li F, Engelmann R, Roberts R, Armato S. Dual energy subtraction and temporal subtraction chest radiography. *J Thorac Imaging*. 2008;23(2):77-85. doi:10.1097/RTI.0b013e318173dd38

8. Johnson TRC. Dual-energy CT: general principles. *AJR Am J Roentgenol*. 2012;199(5 Suppl):S3-8. doi:10.2214/AJR.12.9116

9. Fischbach F, Freund T, Röttgen R, Engert U, Felix R, Ricke J. Dual-energy chest radiography with a flat-panel digital detector: revealing calcified chest abnormalities. *AJR Am J Roentgenol*. 2003;181(6):1519-1524. doi:10.2214/ajr.181.6.1811519

10. Kaza RK, Platt JF, Cohan RH, Caoili EM, Al-Hawary MM, Wasnik A. Dual-energy CT with single- and dual-source scanners: current applications in evaluating the genitourinary tract. *Radiogr Rev Publ Radiol Soc N Am Inc*. 2012;32(2):353-369. doi:10.1148/rg.322115065

11. Euler A, Parakh A, Falkowski AL, et al. Initial Results of a Single-Source Dual-Energy Computed Tomography Technique Using a Split-Filter: Assessment of Image Quality, Radiation Dose, and Accuracy of Dual-Energy Applications in an In Vitro and In Vivo Study. *Invest Radiol*. 2016;51(8):491-498. doi:10.1097/RLI.0000000000000257

12. Yu L, Christner JA, Leng S, Wang J, Fletcher JG, McCollough CH. Virtual monochromatic imaging in dual-source dual-energy CT: radiation dose and image quality. *Med Phys*. 2011;38(12):6371-6379. doi:10.1118/1.3658568

13. Engel KJ, Herrmann C, Zeitler G. X-ray scattering in single- and dual-source CT. *Med Phys*. 2008;35(1):318-332. doi:10.1118/1.2820901

14. Richard S, Siewerdsen JH. Cascaded systems analysis of noise reduction algorithms in dual-energy imaging. *Med Phys*. 2008;35(2):586-601. doi:10.1118/1.2826556

15. Kalender WA, Klotz E, Kostaridou L. An algorithm for noise suppression in dual energy CT material density images. *IEEE Trans Med Imaging*. 1988;7(3):218-224. doi:10.1109/42.7785

16. Okunieff P, Petersen AL, Philip A, et al. Stereotactic Body Radiation Therapy (SBRT) for lung metastases. *Acta Oncol Stockh Swed*. 2006;45(7):808-817. doi:10.1080/02841860600908954

17. Podgorsak EB. *Radiation Physics for Medical Physicists*. Springer International Publishing; 2016. doi:10.1007/978-3-319-25382-4

18. Seppenwoolde Y, Shirato H, Kitamura K, et al. Precise and real-time measurement of 3D tumor motion in lung due to breathing and heartbeat, measured during radiotherapy. *Int J Radiat Oncol Biol Phys*. 2002;53(4):822-834. doi:10.1016/s0360-3016(02)02803-1

19. Huang CY, Tehrani JN, Ng JA, Booth J, Keall P. Six degrees-of-freedom prostate and lung tumor motion measurements using kilovoltage intrafraction monitoring. *Int J Radiat Oncol Biol Phys*. 2015;91(2):368-375. doi:10.1016/j.ijrobp.2014.09.040

20. Bertholet J, Knopf A, Eiben B, et al. Real-time intrafraction motion monitoring in external beam radiotherapy. *Phys Med Biol*. 2019;64(15):15TR01. doi:10.1088/1361-6560/ab2ba8

21. van Herk M, Remeijer P, Rasch C, Lebesque JV. The probability of correct target dosage: dose-population histograms for deriving treatment margins in radiotherapy. *Int J Radiat Oncol Biol Phys*. 2000;47(4):1121-1135. doi:10.1016/s0360-3016(00)00518-6

22. Keall PJ, Kini VR, Vedam SS, Mohan R. Potential radiotherapy improvements with respiratory gating. *Australas Phys Eng Sci Med*. 2002;25(1):1-6. doi:10.1007/BF03178368

23. Murphy MJ, Martin D, Whyte R, Hai J, Ozhasoglu C, Le QT. The effectiveness of breath-holding to stabilize lung and pancreas tumors during radiosurgery. *Int J Radiat Oncol Biol Phys*. 2002;53(2):475-482. doi:10.1016/s0360-3016(01)02822-x

24. Bibault JE, Prevost B, Dansin E, Mirabel X, Lacornerie T, Lartigau E. Image-guided robotic stereotactic radiation therapy with fiducial-free tumor tracking for lung cancer. *Radiat Oncol Lond Engl*. 2012;7:102. doi:10.1186/1748-717X-7-102

25. Hazelaar C, van der Weide L, Mostafavi H, Slotman BJ, Verbakel WFAR, Dahele M. Feasibility of markerless 3D position monitoring of the central airways using kilovoltage projection images: Managing the risks of central lung stereotactic radiotherapy. *Radiother Oncol J Eur Soc Ther Radiol Oncol*. 2018;129(2):234-241. doi:10.1016/j.radonc.2018.08.007

26. Hirai R, Sakata Y, Tanizawa A, Mori S. Real-time tumor tracking using fluoroscopic imaging with deep neural network analysis. *Phys Medica PM Int J Devoted Appl Phys Med Biol Off J Ital Assoc Biomed Phys AIFB*. 2019;59:22-29. doi:10.1016/j.ejmp.2019.02.006

27. Rottmann J, Aristophanous M, Chen A, Court L, Berbeco R. A multi-region algorithm for markerless beam's-eye view lung tumor tracking. *Phys Med Biol*. 2010;55(18):5585-5598. doi:10.1088/0031-9155/55/18/021

28. Mostafavi H, Sloutsky A, Jeung A. Detection and localization of radiotherapy targets by template matching. *Annu Int Conf IEEE Eng Med Biol Soc IEEE Eng Med Biol Soc Annu Int Conf*. 2012;2012:6023-6027. doi:10.1109/EMBC.2012.6347367

29. Cui Y, Dy JG, Sharp GC, Alexander B, Jiang SB. Multiple template-based fluoroscopic tracking of lung tumor mass without implanted fiducial markers. *Phys Med Biol*. 2007;52(20):6229-6242. doi:10.1088/0031-9155/52/20/010

30. Ionascu D, Jiang SB, Nishioka S, Shirato H, Berbeco RI. Internal-external correlation investigations of respiratory induced motion of lung tumors. *Med Phys*. 2007;34(10):3893-3903. doi:10.1118/1.2779941

31. Hoisak JDP, Sixel KE, Tirona R, Cheung PCF, Pignol JP. Correlation of lung tumor motion with external surrogate indicators of respiration. *Int J Radiat Oncol Biol Phys*. 2004;60(4):1298-1306. doi:10.1016/j.ijrobp.2004.07.681

32. Hong JC, Eclov NCW, Yu Y, et al. Migration of implanted markers for image-guided lung tumor stereotactic ablative radiotherapy. *J Appl Clin Med Phys*. 2013;14(2):4046. doi:10.1120/jacmp.v14i2.4046

33. Kupelian PA, Forbes A, Willoughby TR, et al. Implantation and stability of metallic fiducials within pulmonary lesions. *Int J Radiat Oncol Biol Phys*. 2007;69(3):777-785. doi:10.1016/j.ijrobp.2007.03.040

34. Mélanie Gionet. Nouvelles technologies en radio-oncologie. Presented at: Journée scientifique en oncologie; October 21, 2016.

35. van Elmpt W, Landry G, Das M, Verhaegen F. Dual energy CT in radiotherapy: Current applications and future outlook. *Radiother Oncol J Eur Soc Ther Radiol Oncol*. 2016;119(1):137-144. doi:10.1016/j.radonc.2016.02.026

36. Sajja S, Lee Y, Eriksson M, et al. Technical Principles of Dual-Energy Cone Beam Computed Tomography and Clinical Applications for Radiation Therapy. *Adv Radiat Oncol*. 2020;5(1):1-16. doi:10.1016/j.adro.2019.07.013

37. Purdie TG, Bissonnette JP, Franks K, et al. Cone-beam computed tomography for on-line image guidance of lung stereotactic radiotherapy: localization, verification, and intrafraction tumor position. *Int J Radiat Oncol Biol Phys*. 2007;68(1):243-252. doi:10.1016/j.ijrobp.2006.12.022

38. Marchant TE, Moore CJ, Rowbottom CG, MacKay RI, Williams PC. Shading correction algorithm for improvement of cone-beam CT images in radiotherapy. *Phys Med Biol*. 2008;53(20):5719-5733. doi:10.1088/0031-9155/53/20/010

39. Li H, Giles W, Ren L, Bowsher J, Yin FF. Implementation of dual-energy technique for virtual monochromatic and linearly mixed CBCTs. *Med Phys*. 2012;39(10):6056-6064. doi:10.1118/1.4752212

40. Bamberg F, Dierks A, Nikolaou K, Reiser MF, Becker CR, Johnson TRC. Metal artifact reduction by dual energy computed tomography using monoenergetic extrapolation. *Eur Radiol*. 2011;21(7):1424-1429. doi:10.1007/s00330-011-2062-1

41. Zhou C, Zhao YE, Luo S, et al. Monoenergetic imaging of dual-energy CT reduces artifacts from implanted metal orthopedic devices in patients with factures. *Acad Radiol*. 2011;18(10):1252-1257. doi:10.1016/j.acra.2011.05.009

42. Huang JY, Kerns JR, Nute JL, et al. An evaluation of three commercially available metal artifact reduction methods for CT imaging. *Phys Med Biol*. 2015;60(3):1047-1067. doi:10.1088/0031-9155/60/3/1047

43. Schwahofer A, Bär E, Kuchenbecker S, Grossmann JG, Kachelrieß M, Sterzing F. The application of metal artifact reduction (MAR) in CT scans for radiation oncology by monoenergetic extrapolation with a DECT scanner. *Z Med Phys*. 2015;25(4):314-325. doi:10.1016/j.zemedi.2015.05.004

44. Wu M, Keil A, Constantin D, Star-Lack J, Zhu L, Fahrig R. Metal artifact correction for x-ray computed tomography using kV and selective MV imaging. *Med Phys*. 2014;41(12):121910. doi:10.1118/1.4901551

45. Li H, Liu B, Yin FF. Generation of virtual monochromatic CBCT from dual kV/MV beam projections. *Med Phys*. 2013;40(12):121910. doi:10.1118/1.4824324

46. Granton PV, Pollmann SI, Ford NL, Drangova M, Holdsworth DW. Implementation of dual- and triple-energy cone-beam micro-CT for postreconstruction material decomposition. *Med Phys*. 2008;35(11):5030-5042. doi:10.1118/1.2987668

47. Saito M. Potential of dual-energy subtraction for converting CT numbers to electron density based on a single linear relationship. *Med Phys*. 2012;39(4):2021-2030. doi:10.1118/1.3694111

48. Tsukihara M, Noto Y, Hayakawa T, Saito M. Conversion of the energy-subtracted CT number to electron density based on a single linear relationship: an experimental verification using a clinical dual-source CT scanner. *Phys Med Biol*. 2013;58(9):N135-144. doi:10.1088/0031-9155/58/9/N135

49. Saito M, Sagara S. A simple formulation for deriving effective atomic numbers via electron density calibration from dual-energy CT data in the human body. *Med Phys*. 2017;44(6):2293-2303. doi:10.1002/mp.12176

50. Sherertz T, Hoggarth M, Luce J, et al. Prospective evaluation of dual-energy imaging in patients undergoing image guided radiation therapy for lung cancer: initial clinical results. *Int J Radiat Oncol Biol Phys*. 2014;89(3):525-531. doi:10.1016/j.ijrobp.2014.03.004

51. Patel R, Panfil J, Campana M, et al. Markerless motion tracking of lung tumors using dual-energy fluoroscopy. *Med Phys*. 2015;42(1):254-262. doi:10.1118/1.4903892

52. Dhont J, Verellen D, Poels K, et al. Feasibility of markerless tumor tracking by sequential dual-energy fluoroscopy on a clinical tumor tracking system. *Radiother Oncol J Eur Soc Ther Radiol Oncol*. 2015;117(3):487-490. doi:10.1016/j.radonc.2015.08.021

53. Haytmyradov M, Mostafavi H, Wang A, et al. Markerless tumor tracking using fast-kV switching dual-energy fluoroscopy on a benchtop system. *Med Phys*. 2019;46(7):3235-3244. doi:10.1002/mp.13573

54. Jung J, Song SY, Yoon SM, et al. Verification of Accuracy of CyberKnife Tumor-tracking Radiation Therapy Using Patient-specific Lung Phantoms. *Int J Radiat Oncol Biol Phys*. 2015;92(4):745-753. doi:10.1016/j.ijrobp.2015.02.055

55. Nakayama M, Nishimura H, Mayahara H, et al. Clinical log data analysis for assessing the accuracy of the CyberKnife fiducial-free lung tumor tracking system. *Pract Radiat Oncol*. 2018;8(2):e63-e70. doi:10.1016/j.prro.2017.10.014

56. Shiinoki T, Kawamura S, Uehara T, et al. Evaluation of a combined respiratory-gating system comprising the TrueBeam linear accelerator and a new real-time tumor-tracking radiotherapy system: a preliminary study. *J Appl Clin Med Phys*. 2016;17(4):202-213. doi:10.1120/jacmp.v17i4.6114

57. Bowman WA, Robar JL, Sattarivand M. Optimizing dual-energy x-ray parameters for the ExacTrac clinical stereoscopic imaging system to enhance soft-tissue imaging. *Med Phys*. 2017;44(3):823-831. doi:10.1002/mp.12093

58. Bissonnette JP, Balter PA, Dong L, et al. Quality assurance for image-guided radiation therapy utilizing CT-based technologies: a report of the AAPM TG-179. *Med Phys*. 2012;39(4):1946-1963. doi:10.1118/1.3690466

59. Poulsen PR, Cho B, Langen K, Kupelian P, Keall PJ. Three-dimensional prostate position estimation with a single x-ray imager utilizing the spatial probability density. *Phys Med Biol*. 2008;53(16):4331-4353. doi:10.1088/0031-9155/53/16/008

60. Poulsen PR, Cho B, Keall PJ. Real-time prostate trajectory estimation with a single imager in arc radiotherapy: a simulation study. *Phys Med Biol*. 2009;54(13):4019-4035. doi:10.1088/0031-9155/54/13/005

61. Stevens MTR, Parsons DD, Robar JL. Patient specific methods for room-mounted x-ray imagers for monoscopic/stereoscopic prostate motion monitoring. *J Appl Clin Med Phys*. 2017;18(4):40-50. doi:10.1002/acm2.12092

62. Molitoris JK, Diwanji T, Snider JW, et al. Optimizing immobilization, margins, and imaging for lung stereotactic body radiation therapy. *Transl Lung Cancer Res*. 2019;8(1):24-31. doi:10.21037/tlcr.2018.09.25

63. Ehrbar S, Perrin R, Peroni M, et al. Respiratory motion-management in stereotactic body radiation therapy for lung cancer - A dosimetric comparison in an anthropomorphic lung phantom (LuCa). *Radiother Oncol J Eur Soc Ther Radiol Oncol*. 2016;121(2):328-334. doi:10.1016/j.radonc.2016.10.011

64. Wong JW, Sharpe MB, Jaffray DA, et al. The use of active breathing control (ABC) to reduce margin for breathing motion. *Int J Radiat Oncol Biol Phys*. 1999;44(4):911-919. doi:10.1016/s0360-3016(99)00056-5

65. Shirato H, Shimizu S, Kitamura K, et al. Four-dimensional treatment planning and fluoroscopic real-time tumor tracking radiotherapy for moving tumor. *Int J Radiat Oncol Biol Phys*. 2000;48(2):435-442. doi:10.1016/s0360-3016(00)00625-8

66. Stevens MTR, Parsons DD, Robar JL. Continuous monitoring of prostate position using stereoscopic and monoscopic kV image guidance. *Med Phys*. 2016;43(5):2558. doi:10.1118/1.4947295

67. Mueller M, Poulsen P, Hansen R, et al. The markerless lung target tracking AAPM Grand Challenge (MATCH) results. *Med Phys*. 2022;49(2):1161-1180. doi:10.1002/mp.15418

68. ExacTrac 6.2 - Clinical User Guide - English. Published online 2016.

69. Darvish-Molla S, Reno MC, Sattarivand M. Patient-specific pixel-based weighting factor dual-energy x-ray imaging system using a priori CT data. *Med Phys*. 2019;46(2):528-543. doi:10.1002/mp.13354

70. Darvish-Molla S, Spurway A, Sattarivand M. Comprehensive characterization of ExacTrac stereoscopic image guidance system using Monte Carlo and Spektr simulations. *Phys Med Biol*. 2020;65(24):245029. doi:10.1088/1361-6560/ab91d8

71. Wei L, Cappelle C, Ruichek Y, Zann F. GPS and Stereovision-Based Visual Odometry: Application to Urban Scene Mapping and IntelligentVehicle Localization. *Int J Veh Technol*. 2011;2011:1-17. doi:10.1155/2011/439074

72. André Aichert, Nicole Maass, Yu Deuerling-Zheng, et al. Redundancies in x-ray images due to the epipolar geometry for transmission imaging. In: *Proceedings of the Third International Conference on Image Formation in X-Ray Computed Tomography*. ; 2014:333-337.

73. Aichert A, Wang J, Schaffert R, Dörfler A, Hornegger J, Maier A. Epipolar Consistency in Fluoroscopy for Image-Based Tracking. In: *Procedings of the British Machine Vision Conference 2015*. British Machine Vision Association; 2015:82.1-82.10. doi:10.5244/C.29.82

74. Jordan P, West J, Sharda A, Maurer C. SU-GG-J-24: Retrospective Clinical Data Analysis of Fiducial-Free Lung Tracking. *Med Phys*. 2010;37(6Part9):3150-3150. doi:10.1118/1.3468248

75. ExacTrac Vero 3.6 - Clinical User Guide - English. Published online 2018.

76. Epipolar Geometry. OpenCV Open Source Computer Vision. https://docs.opencv.org/3.4/da/de9/tutorial_py_epipolar_geometry.html

77. Mike Sattarivand, Chris Peacock. Real-time markerless stereoscopic lung tumor monitoring with reduced imaging dose using an epipolar constraint. *Med Phys*. 2021;48(8).

78. Papiez L, Langer M. On probabilistically defined margins in radiation therapy. *Phys Med Biol*. 2006;51(16):3921-3939. doi:10.1088/0031-9155/51/16/003

79. Montanaro T, Nguyen DT, Keall PJ, et al. A comparison of gantry-mounted x-ray-based real-time target tracking methods. *Med Phys*. 2018;45(3):1222-1232. doi:10.1002/mp.12765

80. Kalman RE. A New Approach to Linear Filtering and Prediction Problems. *J Basic Eng*. 1960;82(1):35-45. doi:10.1115/1.3662552

81. Alex Becker. Kalman Filter in One Dimension. KalmanFilter.net. https://www.kalmanfilter.net/book.html

82. Hoggarth MA, Luce J, Syeda F, et al. Dual energy imaging using a clinical on-board imaging system. *Phys Med Biol*. 2013;58(12):4331-4340. doi:10.1088/0031-9155/58/12/4331

83. Palmans H, Andreo P, Huq MS, Seuntjens J, Christaki KE, Meghzifene A. Dosimetry of small static fields used in external photon beam radiotherapy: Summary of TRS-483, the IAEA-AAPM international Code of Practice for reference and relative dose determination. *Med Phys*. 2018;45(11):e1123-e1145. doi:10.1002/mp.13208

84. Abeywardhana R, Spurway A, Sattarivand M. Estimation of patient-size dependent imaging dose for stereoscopic/monoscopic real-time kV image guidance in lung and prostate SBRT. *Phys Med Biol*. 2023;68(9). doi:10.1088/1361-6560/acc7f0

85. Rogers DW, Faddegon BA, Ding GX, Ma CM, We J, Mackie TR. BEAM: a Monte Carlo code to simulate radiotherapy treatment units. *Med Phys*. 1995;22(5):503-524. doi:10.1118/1.597552

86. Ding GX, Alaei P, Curran B, et al. Image guidance doses delivered during radiotherapy: Quantification, management, and reduction: Report of the AAPM Therapy Physics Committee Task Group 180. *Med Phys*. 2018;45(5):e84-e99. doi:10.1002/mp.12824

87. Abeywardhana R, MacDonald RL, Sattarivand M. The Effect of Real-Time Imaging Dose on OAR Constraints in Lung SBRT. *Radiother Oncol*. 2023;186:S120-S121. doi:10.1016/S0167-8140(23)89375-6

88. Poulsen PR, Cho B, Keall PJ. A method to estimate mean position, motion magnitude, motion correlation, and trajectory of a tumor from cone-beam CT projections for image-guided radiotherapy. *Int J Radiat Oncol Biol Phys*. 2008;72(5):1587-1596. doi:10.1016/j.ijrobp.2008.07.037

89. Li R, Fahimian BP, Xing L. A Bayesian approach to real-time 3D tumor localization via monoscopic x-ray imaging during treatment delivery. *Med Phys*. 2011;38(7):4205-4214. doi:10.1118/1.3598435

90. Chung H, Poulsen PR, Keall PJ, Cho S, Cho B. Reconstruction of implanted marker trajectories from cone-beam CT projection images using interdimensional correlation modeling. *Med Phys*. 2016;43(8):4643. doi:10.1118/1.4958678

91. Shieh CC, Caillet V, Dunbar M, et al. A Bayesian approach for three-dimensional markerless tumor tracking using kV imaging during lung radiotherapy. *Phys Med Biol*. 2017;62(8):3065-3080. doi:10.1088/1361-6560/aa6393

92. Nguyen DT, Keall P, Booth J, Shieh CC, Poulsen P, O'Brien R. A real-time IGRT method using a Kalman filter framework to extract 3D positions from 2D projections. *Phys Med Biol*. 2021;66(21):214001. doi:10.1088/1361-6560/ac06e3

93. Depuydt T, Poels K, Verellen D, et al. Initial assessment of tumor tracking with a gimbaled linac system in clinical circumstances: a patient simulation study. *Radiother Oncol J Eur Soc Ther Radiol Oncol*. 2013;106(2):236-240. doi:10.1016/j.radonc.2012.12.015

94. Keall PJ, Sawant A, Berbeco RI, et al. AAPM Task Group 264: The safe clinical implementation of MLC tracking in radiotherapy. *Med Phys*. 2021;48(5). doi:10.1002/mp.14625

95. Engels B, Soete G, Verellen D, Storme G. Conformal Arc Radiotherapy for Prostate Cancer: Increased Biochemical Failure in Patients With Distended Rectum on the Planning Computed Tomogram Despite Image Guidance by Implanted Markers. *Int J Radiat Oncol*. 2009;74(2):388-391. doi:10.1016/j.ijrobp.2008.08.007

96. Haytmyradov M, Mostafavi H, Cassetta R, et al. Adaptive weighted log subtraction based on neural networks for markerless tumor tracking using dual-energy fluoroscopy. *Med Phys*. 2020;47(2):672-680. doi:10.1002/mp.13941

97. Romadanov I, Abeywardhana R, Sattarivand M. Adaptive dual-energy algorithm based on pre-calibrated weighting factors for chest radiography. *Phys Med Biol*. 2022;67(9):095011. doi:10.1088/1361-6560/ac6201